TABLE OF CONTENTS

	Page	
SUMMARY	1	1/A5
INTRODUCTION	1	1/A5
SYMBOLS	3	1/A7
MATHEMATICAL MODEL DEVELOPMENT	9	1/A13
Coordinate System	9	1/A13
"Coarse" Assembly Equations	10	1/A14
Vernier Assembly Equations	16	1/B6
Combined Equations of Motion	18	1/B8
Magnetic Actuator Centering Errors	19	1/B9
Magnetic Actuator Models	20	1/B10
Roll Motor Disturbance Model	20	1/B10
Cable Forces and Torques	21	1/B11
Gimbal Torquer Models	22	1/B12
CONTROL SYSTEMS DESIGN	24	1/B14
"Coarse" Gimbal Control System	24	1/B14
Magnetic Actuator Control System	26	1/C2
SENSOR MODELS	31	1/C7
PAYLOAD ATTITUDE STATE ESTIMATORS	32	1/C8
SIMULATION DESCRIPTION	32	1/C8
NUMERICAL RESULTS AND DISCUSSION	35	1/C11
CONCLUSIONS	37	1/C13
REFERENCES	39	1/D1
TABLES	41	1/D
FIGURES	50	1/D14

ceter 830-H-14 NAS1.26:3040

NOV 7 8 1978

NASA Contractor Report 3040

ORIGINAL
COMPLETED

Nonlinear Analysis and Performance Evaluation of the Annular Suspension and Pointing System (ASPS)

Suresh M. Joshi

GRANT NSG-1241
AUGUST 1978

NASA

63

stem 830-H-14 NAS1.26:3040

NASA Contractor Report 3040

Nonlinear Analysis and Performance Evaluation of the Annular Suspension and Pointing System (ASPS)

Suresh M. Joshi
Old Dominion University Research Foundation
Norfolk, Virginia

Prepared for
Langley Research Center
under Grant NSG-1241

NASA
National Aeronautics
and Space Administration

Scientific and Technical
Information Office

1978

BLANK PAGE

NONLINEAR ANALYSIS AND PERFORMANCE EVALUATION OF THE ANNULAR SUSPENSION AND POINTING SYSTEM (ASPS)

By

Suresh M. Joshi*

SUMMARY

The Annular Suspension and Pointing System (ASPS) can provide highly accurate fine pointing for a variety of solar-, stellar-, and Earth-viewing missions. In this report, a detailed nonlinear mathematical model is developed for the ASPS/Space Shuttle system. The equations are augmented with models of components such as magnetic actuators and gimbal torquers. Control systems and payload attitude state estimators are designed in order to obtain satisfactory pointing performance, and statistical pointing performance is predicted in the presence of measurement noise and disturbances.

INTRODUCTION

The Annular Suspension and Pointing System (ASPS) holds the promise of providing very high payload pointing accuracy and stability during space shuttle orbital missions. The basic concept of ASPS was suggested in reference 1, and was developed in reference 2, along with preliminary results on statistical pointing performance based on a linearized mathematical model. A more elaborate linear analysis was carried out in references 3 and 4 in which a detailed model of the ASPS/Space Shuttle system was developed and used. Payload attitude measurement noise and state estimators were also included in references 3 and 4. The linear analyses used linear mathematical models for stochastic crew motion disturbances.

---

* Research Assistant Professor, School of Engineering, Old Dominion University, Norfolk, Virginia 23508.

The physical system, however, contains a number of nonlinearities. The nonlinearities include inherent trigonometric nonlinearities, magnetic actuator nonlinearities, gimbal friction and torquer nonlinearities, etc. It was therefore necessary to include these nonlinearities in order to more accurately predict the performance of ASPS. Detailed information regarding ASPS components (e.g., magnetic actuator models) also became available from the Sperry Flight Systems, under contract NAS1-14214, during the course of this work, and was used in the nonlinear mathematical model.

The ASPS (fig. 1) consists of an elevation gimbal and a lateral gimbal for "coarse" pointing. Magnetic suspension and fine pointing actuators are provided in the vernier assembly and generate fine pointing control torques. The payload or vernier assembly (VA), which consists of an annular rim (made of magnetic material) attached to a payload mounting plate (PMP), is levitated by the magnetic actuators of the VA. The payload instrument is mounted on the PMP. A noncontacting optical data coupler is used for transmission of data between VA and the Space Shuttle pallet. A battery pack mounted on the PMP supplies the payload power and eliminates the necessity of any cables. As a result of design evolution, the present version of ASPS, which is shown in figure 1, is somewhat different from the ASPS used in references 3 and 4 (although mathematical descriptions do not significantly differ). The functions of various components remain the same, and are described in references 2, 3, and 4. The magnetic actuator configuration is also different from that used in references 2, 3, and 4. There are three axial actuator stations (A, B, C) spaced 120° apart and two radial actuator stations (U,V) spaced 90° apart, as shown in figure 2. Roll motor station W consists of two segments, one inside and one outside the rim. The system considered in this study has been sized for payloads up to 600 kg with Z-axis center of mass offsets up to 1.5 m. The magnetic suspension actuators use bias current linearization to remove the current squared nonlinearity. To compensate for the inverse-gap-squared relationship, a signal proportional to the gap is used to multiply coil currents. A segmented two-phase solid iron rotor AC induction motor controls the roll rotational servo. Proximity sensors

are provided at each axial and radial actuator station, as well as at the roll motor station to compensate for radial gap. The "coarse" gimbal torquers are permanent magnet, two-phase brushless DC type.

The objectives of this study are

- Development of complete nonlinear equations of motion for ASPS/Space Shuttle system.
- Inclusion of all available component models (e.g., magnetic actuators, "coarse" gimbal torquers, etc.).
- Design of control systems for the vernier assembly and the "coarse" gimbals.
- Design of payload attitude state estimators.
- Prediction of statistical pointing performance via digital computer simulation.

The analysis presented here is based on rigid-body models, and thus does not contain representations of structural modes.

SYMBOLS

A, B, C	Axial actuator stations
A, $\bar{A}$, A_g, A_{ij}	Coefficient matrices
A_j	Point on lateral gimbal representing actuator station j (j = A, B, C, U, V)
B_j	Point on vernier assembly corresponding to A_j
C_F, C_T	Coefficient matrices used in controller design
C_g	"Coarse" gimbal control matrix
$C_p(x)$	Cross product matrix of x
D_{ij}	Transformation matrix from i- to j-coordinate system
d	Five-dimensional vector appearing in eq. (67)
E	Body rate to Euler rate transformation matrix

e_i	Unit vector in i direction (i = 1, 2, 3)
F	Magnetic actuator force vector (total)
F_{ai}	Magnetic actuator axial forces
F_{bias}	Cable bias force
F_{ca}	Total cable force
F_{cs}	Cable spring force
F_j	Force vector generated by actuator station j
F_{lei}	Force exerted by lateral gimbal on elevation gimbal contact surface
F_r	Reactive force acting on coarse assembly
F_{rd}	Radial disturbance force due to roll motor
F_{ri}	Magnetic actuator radial forces
F_s	Force acting on shuttle
F_T	Tangential force due to roll motor
f	Force vector defined in eq. (78)
f_c	Cogging frequency
f_r	Ripple frequency
I_0	Inertia matrix of shuttle
I_1	Inertia matrix of elevation gimbal
I_2	Inertia matrix of lateral gimbal
I_v	Inertia matrix of vernier (payload) assembly
J	Performance function
K	Control gain
L	Vector functions of ω_o, ϕ, θ, $\dot{\phi}$, $\dot{\theta}$, α_o, α_v, ω_v
L_g	Proportional gain for gimbal control system
M_p	External moment acting on shuttle
M_v	Magnetic actuator torque acting on vernier assembly

m	$m_0 + m_1 + m_2$
m_0	Mass of shuttle
m_1	Mass of elevation gimbal
m_2	Mass of lateral gimbal
m_v	Mass of vernier assembly
O	Origin of 2"-frame; also the point fixed to lateral gimbal which is the nominal position of payload mounting plate center
O_i	Origin of i-frame
O_v	Center of payload mounting plate
P	Center of mass of shuttle
P_c	Combined center of mass of shuttle and "coarse" gimbals
P_e	Center of elevation gimbal axis
P_ℓ	Center of lateral gimbal axis
P_r	Percent ripple
R_{cm_1}	Position of elevation gimbal c.m. relative to P in O-system
R_{cm_2}	Position of lateral gimbal c.m. relative to P in O-system
R_{cma}	Position of lateral gimbal c.m. relative to P_e in l-system
R_{cmm}	$m_1 R_{cm_1} + m_2 R_{cm_2}$
$\overline{R}_{\ell ei}$	Position of a point on the mutual contact surface between lateral and elevation gimbals relative to P_e
r	Radius of payload mounting plate used in magnetic actuator torque expressions
$\overline{r}_c$	Position of combined c.m. of shuttle and two gimbals relative to O_i
r_{cm_1}	Position of elevation gimbal c.m. relative to P_e in 1'-system

r_{cm_2}	Position of lateral gimbal c.m. relative to P_ℓ in 2'-system
r_{cmv}	Position of vernier assembly c.m. in v-system
r_d	Position of P_ℓ relative to P_e in 1'-system
r_e	Position of payload mounting plate center relative to O in 2"-system
r_j	Position of actuator station j in 2"-system
r_ℓ	Position of O relative to lateral c.m. in 2-system
$\bar{r}_{\ell ei}$	Position of a point on the mutual contact surface between lateral and elevation gimbals relative to P_ℓ
$\bar{r}_p$	Position of P relative to O_i
$\bar{r}_v$	Position of vernier assembly c.m. relative to O_i
$\bar{r}_1$, $\bar{r}_2$	Positions of c.m. of elevation and lateral gimbals relative to O_i
$\bar{r}_1'$, $\bar{r}_2'$	Positions of P_e and P_ℓ relative to O_i
$r_{\phi vc}$	Rate command for ϕ_v
T_{bias}	Bias cable torque
T_c	Cable torque acting on vernier assembly
T_{ca}	Cable torque acting on lateral gimbal
T_{cog}	Cogging torque
T_{cogo}	Peak cogging torque
T_{com}	Commanded torque
T_d	Disturbance torque
T_f	Gimbal friction torque
T_{fo}	Peak or Coulomb friction torque
T_{fil}	Estimator update interval
T_i	Noise-generation time interval

T_{RCJ}	Reaction control jet torque
T_r	Reaction torque acting on lateral gimbal
T_{ripple}	Ripple torque
T_1	Elevation gimbal torquer torque
$T_{1_{com}}$	Elevation gimbal commanded torque
T_2	Lateral gimbal torquer torque
$T_{2_{com}}$	Lateral gimbal commanded torque
$T_i(\nu)$	Transformation matrix for ν radians rotation about axis i
T_v	Magnetic torque acting on vernier assembly
T_3'	$T_3(45°)$
U, V	Radial actuator stations
(X, Y, Z)	Denotes coordinate frames; subscripts are described in the text
z	Integrator state variable
α_i	Coefficient matrices
α_o	Attitude vector of shuttle
α_v	Attitude vector of vernier assembly
α_{vr}	Attitude vector of vernier assembly relative to lateral gimbal
β	Incremental gimbal angle vector
β_c	Commanded gimbal angle vector
β_i	Vector functions of state variables
Γ_1, Γ_2	Matrices used in payload following controller design
γ	Gimbal torquer angle
ΔA, ΔB, etc.	Linearized center errors and gimbal angles [defined in eq. (67)]
δ_j	Centering error vector at actuator station j

λ	Desired decay characteristic
ρ	Damping ratio
ρ_{Aj}	Position of actuator station j relative to O
ρ_{Bj}	Position of point on rim corresponding to A_j relative to O_v
$\bar{\rho}_c$	Position of combined c.m. of shuttle and two gimbals relative to P
$\bar{\rho}_{cmv}$	Position of vernier assembly c.m. relative to O_v
$\bar{\rho}_{cm_1}$	Position of elevation gimbal c.m. relative to P_e
$\bar{\rho}_{cm_2}$	Position of lateral gimbal c.m. relative to P_ℓ
$\bar{\rho}_d$	Position of P_ℓ relative to P_e
$\bar{\rho}_e$	Position of O_v relative to O
$\bar{\rho}_\ell$	Position of O relative to lateral gimbal c.m.
$\bar{\rho}_1$, $\bar{\rho}_2$	Positions of elevation and lateral gimbal c.m. relative to P
$\bar{\rho}'_1$, $\bar{\rho}'_2$	Positions of P_e and P_ℓ relative to P
τ_{se}	Torque exerted by shuttle on elevation gimbal
(ϕ, θ)	Elevation and lateral gimbal angles
$(\phi_o, \theta_o, \psi_o)$	Components of α_o
$(\phi_v, \theta_v, \psi_v)$	Components of α_v
$\phi_{vc}, \theta_{vc}, \psi_{vc}$	Commanded values of ϕ_v, θ_v, ψ_v
$(\phi_{vr}, \theta_{vr}, \psi_{vr})$	Components of α_{vr}
Ω_{vr}	Angular velocity vector of vernier assembly relative to lateral gimbal
Ω_1	Angular velocity of elevation gimbal relative to shuttle
Ω_2	Angular velocity of lateral gimbal relative to elevation gimbal
ω	Natural frequency

$\bar{\omega}_0$, $\bar{\omega}_1$, $\bar{\omega}_2$	Angular velocities of shuttle, lateral, and elevation gimbals relative to i-frame
$\bar{\omega}_v$	Angular velocity of vernier assembly relative to i-frame
ω'_{1_B}	Angular velocity of 1'-frame
ω'_{2_B}	Angular velocity of 2'-system
ζ_{jv}	Position of actuator station j in v-system

An overhead bar denotes a vector quantity and corresponding operations indicate vector operations. (Overhead bars are not used to denote vectors in the Euclidian sense.) Superscripts "T" and "-1" denote transpose and inverse, respectively. One and two overhead dots denote the first and second time derivatives, and an overhead "^" denotes the estimated value of a variable.

MATHEMATICAL MODEL DEVELOPMENT

Coordinate System

Referring to figure 3 $(X_iY_iZ_i)$ is an inertial coordinate system centered at O_i. $(X_0Y_0Z_0)$ is a shuttle-fixed system centered at P, the center of mass of the shuttle. $(X'_1Y'_1Z'_1)$ is a system fixed to the elevation gimbal, with origin at P_e, the center of the elevation gimbal rotation axis. It is obtained from $(X_0Y_0Z_0)$ by one positive rotation ϕ (elevation gimbal angle) about the X_0 axis. Coordinate system $(X_1Y_1Z_1)$ is also fixed to the elevation gimbal and is parallel to the $(X'_1Y'_1Z'_1)$ system. It is centered at the elevation gimbal center of mass. System $(X'_2Y'_2Z'_2)$ is obtained by one positive rotation θ (lateral gimbal angle) about the Y_1 axis, and is fixed to the lateral gimbal. Its origin is the center, P_g, of the gimbal rotation axis. System $(X_2Y_2Z_2)$, which is also fixed to the lateral gimbal, is parallel to $(X'_2Y'_2Z'_2)$ and has the lateral gimbal center of mass as its origin. $(X''_2Y''_2Z''_2)$ is a system fixed to the lateral gimbal which is parallel to $(X_2Y_2Z_2)$. Its origin lies at O, the center of the lateral gimbal plate, which is also the nominal position of the center (O_v) of the payload mounting plate (PMP). $(X_vY_vZ_v)$ is a coordinate system fixed

to the vernier assembly (VA), and its origin is the center, O_v, of the PMP.

"Coarse" Assembly Equations

The "coarse" assembly consists of space shuttle, elevation gimbal, and lateral gimbal. Equations of motion for the "coarse" assembly can be derived by applying the method given in reference 5 (pp. 374-377) for a system of rigid bodies. "Coarse" assembly translation is given by:

$$m \ddot{\bar{r}}_c = \bar{F}_r + \bar{F}_s \tag{1}$$

where $m = m_0 + m_1 + m_2$, and $\bar{r}_c$ is the position of the combined c.m. of the space shuttle, elevation gimbal, and lateral gimbal relative to O_i. $\bar{F}_r$ is the total reactive force acting on the "coarse" assembly, and $\bar{F}_s$ is the sum of other forces acting on the shuttle. $\bar{F}_r$ consists of magnetic actuator force and cable force. The latter is present only when a cable is used for data transmission as a backup for the optical data coupler. Since

$$\bar{r}_c = \bar{r}_p + \bar{\rho}_c \tag{2}$$

and

$$\bar{\rho}_c = \frac{1}{m} (m_1 \bar{\rho}_1 + m_2 \bar{\rho}_2) \tag{3}$$

equation (1) becomes

$$m \ddot{\bar{r}}_p + m_1 \ddot{\bar{\rho}}_1 + \bar{m}_2 \ddot{\bar{\rho}}_2 = \bar{F}_r + \bar{F}_s \tag{4}$$

(see fig. 3 for explanation).

"Coarse" assembly rotational equations are given by

$$\bar{H}_p = \bar{M}_p - \bar{\rho}_c \times m \ddot{\bar{r}}_p \tag{5}$$

where H_p is the angular momentum with P as the reference point or

$$H_p = \bar{I}_0 \bar{\omega}_0 + \bar{I}_1 \bar{\omega}_1 + \bar{I}_2 \bar{\omega}_2 + \bar{\rho}_1 \times m_1 \dot{\bar{\rho}}_1 + \bar{\rho}_2 \times m_2 \dot{\bar{\rho}}_2 \tag{6}$$

where I_1 and I_2 are the inertia matrices of the elevation and lateral gimbals relative to the 1- and 2-system, as observed by an observer rotating with the 0-frame. That is

$$I_1 = D_{01}^T I_{1_B} D_{01} \quad , \quad I_2 = D_{02}^T I_{2_B} D_{02} \tag{7}$$

where I_{1_B} and I_{2_B} are inertia matrices of elevation and lateral gimbals relative to the 1-frame and 2-frame, respectively. M_p is the torque exerted on the "coarse" assembly.

$$\omega_1 = \omega_0 + D_{01}^T \Omega_1 = \omega_0 + \Omega_1 \tag{8}$$

$$\omega_2 = \omega_0 + \Omega_1 + D_{02}^T \Omega_2 = \omega_0 + \Omega_1 + D_{01}^T \Omega_2 \tag{9}$$

Using the notation

$$\bar{H}_i = \bar{I}_i \bar{\omega}_i$$

$$\dot{\bar{H}}_p = \dot{\bar{H}}_0 + \dot{\bar{H}}_1 + \dot{\bar{I}}_2 + \bar{\rho}_1 \times m_1 \ddot{\bar{\rho}}_1 + \bar{\rho}_2 \times m_2 \ddot{\bar{\rho}}_2 = \bar{M}_p - \bar{\rho}_c \times m \ddot{\bar{r}}_p \tag{10}$$

$$\dot{\bar{H}}_i = (\dot{\bar{H}}_i)_r + \bar{\omega}_0 \times \bar{H}_i, \quad i = 0,1,2 \tag{11}$$

where $(\dot{\bar{H}}_i)_r$ is the derivative of $\bar{H}_i$ relative to the 0-frame, expressed along 0-coordinate system,

$$(\dot{\bar{H}}_i)_r = I_i \dot{\omega}_i + \dot{I}_i \omega_i \quad , \quad i = 0,1,2 \tag{12}$$

$$\ddot{\bar{\rho}}_i = (\ddot{\bar{\rho}}_i)_r + 2\bar{\omega}_0 \times (\dot{\bar{\rho}}_i)_r + \bar{\omega}_0 \times (\bar{\omega}_0 \times \bar{\rho}_i) + \dot{\bar{\omega}}_0 \times \rho_i, \quad i = 1,2 \tag{13}$$

But

$$\bar{\rho}_1 = \bar{\rho}_1' + \bar{\rho}_{cm_1}, \qquad \bar{\rho}_2 = \bar{\rho}_1' + \bar{\rho}_d + \bar{\rho}_{cm_2} \tag{14}$$

$$(\dot{\bar{\rho}}_1')_r = (\ddot{\bar{\rho}}_1')_r = 0$$

and

$$(\bar{\rho}_1)_r = \rho_1' + D_{01}^T r_{cm_1} \triangleq R_{cm_1} \tag{15}$$

$$(\bar{\rho}_d)_r = r_d$$

$$(\bar{\rho}_2)_r = \rho_1' + D_{01}^T r_d + D_{02}^T r_{cm_2} \triangleq R_{cm_2} \tag{16}$$

Components of vector derivatives $\ddot{\bar{\rho}}_1$, $\ddot{\bar{\rho}}_2$ can therefore be evaluated as in equation (13) along the 0-axes to obtain

$$\ddot{\bar{\rho}}_1 = \alpha_1 \dot{\omega}_0 + \alpha_2 \ddot{\phi} + \beta_1 \tag{17}$$

$$\ddot{\bar{\rho}}_2 = \alpha_3 \dot{\omega}_0 + \alpha_4 \ddot{\phi} + \alpha_5 \ddot{\theta} + \beta_2 \tag{18}$$

where matrices α_i, β_i are functions of ω_0, ϕ, θ, $\dot{\phi}$, and $\dot{\theta}$.

"Coarse" assembly rotational equations of motion are then obtained by substituting for $m \ddot{\bar{r}}_p$ from equation (4), and for $\ddot{\bar{\rho}}_1$ and $\ddot{\bar{\rho}}_2$ from equations (17) and (18), into equation (10):

$$A_{11} \dot{\omega}_0 + A_{12} \ddot{\phi} + A_{13} \ddot{\theta} + L_{\omega_0} = M_p - \frac{1}{m} C_p(R_{cmm})(D_{02}^T F_r + F_s) \tag{19}$$

where matrices A_{ij} and L_{ω_0} are functions of ω_0, ϕ, θ, $\dot{\phi}$, $\dot{\theta}$, and

$$R_{cmm} = m_1 R_{cm_1} + m_2 R_{cm_2} \tag{20}$$

To obtain complete equations of motion for the "coarse" assembly, equations for elevation and lateral gimbals must also be derived. In these derivations, forces acting at the contact surfaces between shuttle and elevation gimbal, and between elevation and lateral gimbals, must be considered. Forces exerted by the elevation gimbal on the lateral gimbal at their mutual contact surface are assumed to be acting radially, i.e., they produce no torque about the lateral gimbal axis of rotation. Similarly, forces exerted by the shuttle on the elevation gimbal at their mutual contact surface are assumed to produce no torque about the X_1'-axis. Equal and opposite reactive forces act on corresponding bodies at contact surfaces. Since these internal forces must be eliminated from the equations of motion, it is convenient to derive lateral gimbal equations first. Let $\bar{F}_{\ell ei}$ be a force exerted by the lateral gimbal on the elevation gimbal at point $\bar{r}_{\ell ei}$ (with respect to 2'-system) located on the contact surface ($i = 1,2,3\ldots$). Force $-\bar{F}_{\ell ei}$ is exerted by the elevation gimbal on the lateral gimbal.

Lateral gimbal translation equation is

$$m_2 \ddot{\bar{r}}_2 = F_r - \sum \bar{F}_{\ell ei} \tag{21}$$

But

$$\bar{r}_2 = \bar{r}_p + \bar{\rho}_2 \tag{22}$$

Substituting for $\bar{r}_2$ into equation (21), and for $\ddot{\bar{r}}_p$ from equation (4),

$$\sum F_{\ell ei} = \left(1 - \frac{m_2}{m}\right) \bar{F}_r + \frac{m_1 m_2}{m} \ddot{\bar{\rho}}_1$$

$$+ m_2 \left(\frac{m_2}{m} - 1\right) \ddot{\bar{\rho}}_2 - \frac{m_2}{m} \bar{F}_s \tag{23}$$

It is convenient to derive lateral gimbal rotation equations in the 2'-system. Let I'_{2_B} be the inertia matrix of the lateral gimbal relative to the 2'-system. Then

$$H_2 = I'_{2_B}\, \omega_{2_B} \tag{24}$$

where

$$\omega'_{2_B} = D_{02}\, \omega_0 + D_{12}\, \Omega_1 + \Omega_2 \tag{25}$$

$$(\dot{\bar{H}}_2)_r + \bar{\omega}'_{2_B} \times (\bar{H}_2)_r = \bar{T}_r - \bar{r}_{\ell ei} \times \bar{F}_{\ell ei} + \bar{T}_2 - \bar{\rho}_{cm_2} \times m_2\, \ddot{\bar{r}}'_2 \tag{26}$$

where $\bar{T}_r$ is the reaction torque (consisting of magnetic torque and cable torque), and $\bar{T}_2$ is the torquer torque. $\bar{r}'_2$ is the position vector of P_ℓ relative to O_i.

$$\bar{r}'_2 = \bar{r}_p + \bar{\rho}_2 - \bar{\rho}_{cm_2} \tag{27}$$

After evaluating $\ddot{\bar{r}}'_2$ in a way similar to equation (13), and simplifying

$$A'_{31}\, \dot{\omega}_0 + A'_{32}\, \ddot{\phi} + A'_{33}\, \ddot{\theta} + L'_\theta = T_r + T_2 - \left(\sum r_{\ell ei} \times F_{\ell ei}\right) - \frac{m_2}{m} C_p(r_{cm_2})(F_r + D_{02}\, F_s) \tag{28}$$

Equation (28) is obtained along the 2'-system. Matrices A_{ij} and L'_θ are functions of ω_0, ϕ, θ, $\dot{\phi}$, and $\dot{\theta}$. Equation (28) gives the value of $\sum r_{\ell ei} \times F_{\ell ei}$ (along the 2'-coordinate system). Since forces $F_{\ell ei}$ do not produce torque about the Y'_2 axis, the Y'_2 component of $\sum r_{\ell ei} \times F_{\ell ei}$ is zero. Thus the lateral gimbal equation is

$$A_{31}\,\dot{\omega}_0 + A_{32}\,\ddot{\phi} + A_{33}\,\ddot{\theta} + L_\theta = e_2^T\,(T_r + T_2)$$

$$- \frac{m_2}{m}\, e_2^T\, C_p(r_{cm_2})(F_r + D_{02}\, F_s) \qquad (29)$$

where

$$A_{3j} = e_2^T\, A'_{3j}\ , \quad L_\theta = e_2^T\, L'_\theta$$

Elevation gimbal rotation equations are conveniently written in the 1'-system. Let

$$H_1 = I'_{1B}\,\omega'_{1B} \qquad (30)$$

where I'_{1B} is the inertia matrix of the elevation gimbal relative to the 1'-system.

$$\omega'_{1B} = D_{01}\,\omega_0 + \Omega_1 \qquad (31)$$

$$\dot{(\bar{H}_1)}_r + \bar{\omega}'_{1B} \times \bar{H}_1 = \bar{R}_{\ell ei} \times \bar{F}_{\ell ei} + \bar{T}_1 + \bar{\tau}_{se} - \bar{\rho}_{cm_1} \times m_1\, \ddot{\bar{r}}'_1 - \bar{T}_2 \qquad (32)$$

where $\bar{R}_{\ell ei}$ is the point of application of force $\bar{F}_{\ell ei}$ exerted by the lateral gimbal at the contact surface, and $\bar{\tau}_{se}$ is the torque due to forces exerted by the shuttle at the elevation gimbal-shuttle contact surface. $\bar{T}_1$ is the torque exerted by the torquer, and $-\bar{T}_2$ is the reaction torque exerted by the lateral gimbal torquer

$$\bar{R}_{\ell ei} = \bar{\rho}_d + \bar{r}_{\ell ei} \qquad (33)$$

$$\dot{(\bar{H}_1)}_r + \bar{\omega}'_{1B} \times \bar{H}_1 = \bar{\rho}_d \times \bar{F}_{\ell ei} + \sum \bar{r}_{\ell ei} \times \bar{F}_{\ell ei} + \bar{T}_1$$

$$- \bar{\rho}_{cm_1} \times m_1\, \ddot{\bar{r}}'_1 + \bar{\tau}_{se} - \bar{T}_2 \qquad (34)$$

$\bar{\tau}_{se}$ has no component along the X_1' axis

$$\bar{r}_1' = \bar{r}_p + \bar{\rho}_1 - \bar{\rho}_{cm_1} \tag{35}$$

The elevation gimbal equation can be obtained by substituting from equation (28) for $\sum \bar{r}_{\ell ei} \times \bar{F}_{\ell ei}$, and from equation (23) for $\sum \bar{F}_{\ell ei}$, after evaluating $\bar{\rho}_{cm_1} \times m_1 \ddot{\bar{r}}_1'$ as in the case of the lateral gimbal, and taking only the first components

$$\begin{aligned} A_{21}\,\dot{\omega}_0 + A_{22}\,\ddot{\phi} + A_{23}\,\ddot{\theta} + L_\phi = e_1^T \Big[& T_1 + D_{12}^T\, T_r \\ & - C_p \left(\frac{m_2}{m} R_{cma} + \frac{m_1}{m} r_{cm_1} \right) \\ & \cdot \left(D_{12}^T\, F_r + D_{01}\, F_s \right) \\ & + C_p(r_d)\, D_{12}^T\, F_r \Big] \end{aligned} \tag{36}$$

where

$$R_{cma} = r_d + D_{12}^T\, r_{cm_2} \tag{37}$$

Vector coefficients A_{ij} and L_ϕ are functions of ω_0, ϕ, θ, $\dot{\phi}$, and $\dot{\theta}$. Thus equations (19), (29), and (36) define complete rotational motion of the "coarse" assembly.

Vernier Assembly Equations

Let $\bar{r}_v$ be the position of vernier assembly (VA) center of mass relative to O_i. Then

$$m_v \ddot{\bar{r}}_v = -\bar{F}_r \tag{38}$$

But

$$\bar{r}_v = \bar{r}_p + \bar{\rho}_2 + \bar{\rho}_\ell + \bar{\rho}_e + \bar{\rho}_{cmv} \tag{39}$$

$\ddot{\bar{\rho}}_\ell$ can be evaluated as in equation (13). It is convenient to evaluate it along the 2'-coordinates. $\ddot{\bar{\rho}}_{cmv}$ can be conveniently evaluated along the v-system:

$$\ddot{\bar{\rho}}_{cmv} = \dot{\bar{\omega}}_v \times \bar{\rho}_{cmv} + \bar{\omega}_v \times (\bar{\omega}_v \times \bar{\rho}_{cmv}) \tag{40}$$

$\ddot{\bar{\rho}}_e$, the acceleration of PMP center relative to 2"-frame, can be evaluated along 2"-coordinates as in equation (13). Substitution and simplification yield the following VA translation equation along the 2"-system:

$$\ddot{r}_e + H_{11}\dot{\omega}_0 + H_{12}\ddot{\phi} + H_{13}\ddot{\theta} + H_{14}\dot{\omega}_v + L_v = -\left(\frac{1}{m_v} + \frac{1}{m}\right)F_r - \frac{1}{m} D_{02} F_s \tag{41}$$

where H_{1j} and L_v are functions of ω_0, $\dot{\phi}$, $\dot{\theta}$, ω_v, α_0, ϕ, θ, α_v, and r_e.

Defining

$$H_v = I_v \omega_v \tag{42}$$

where I_v is the VA inertia matrix with respect to the v-system

$$I_v \dot{\omega}_v + \omega_v \times (I_v \omega_v) = T_v + T_c - \bar{\rho}_{cmv} \times m_v \ddot{\bar{r}}_v \tag{43}$$

where T_v and T_c are magnetic actuator and cable torques in v-system. Substituting for $m_v \ddot{\bar{r}}_v$ from equation (38) and expressing along 2"-coordinates results in

$$\dot{\omega}_v = I_v^{-1}\Big[-C_p(\omega_v)\ I_v\ \omega_v + T_v - C_p(r_{cmv}) \times (F_v - D_{2_v}\ F_{ca}) + T_c\Big] \tag{44}$$

Combined Equations of Motion

The "coarse" assembly equations have the form:

$$\bar{A}\begin{bmatrix}\dot{\omega}_0\\ \ddot{\phi}\\ \ddot{\theta}\end{bmatrix} = y \tag{45}$$

where $\bar{A}$ is a 5×5 matrix and y is a 5×1 vector of functions of ω_0, $\dot{\phi}$, $\dot{\theta}$, ϕ, and θ, and the forcing functions. These equations can be solved for $(\dot{\omega}_0^T, \ddot{\phi}, \ddot{\theta})^T$ by inverting A:

$$(\dot{\omega}_0^T, \ddot{\phi}, \ddot{\theta})^T = A^{-1}\ y \tag{46}$$

Other equations are

$$\dot{\alpha}_0 = E_0^{-1}\ \omega_0 \tag{47}$$

$$\frac{d}{dt}\phi = \dot{\phi} \tag{48}$$

$$\frac{d}{dt}\theta = \dot{\theta} \tag{49}$$

$$\frac{d}{dt}r_e = \dot{r}_e \tag{50}$$

$$\dot{\alpha}_v = E_v^{-1}\omega_v \tag{51}$$

where E_0 and E_v are Euler to body rate transformation matrices for shuttle and VA.

Equations (46) to (51), along with (41) and (44) represent complete rigid-body equations of motion for the ASPS/space shuttle.

Magnetic Actuator Centering Errors

Let $\bar{\rho}_{Aj}$ denote the position of actuator station j relative to O, the lateral gimbal plate center, and $\bar{\rho}_{Bj}$ denote the position of corresponding point B_j in the vernier assembly, relative to O_v. Then the magnetic actuator centering errors are given by

$$\delta_j = -\bar{\rho}_{Aj} + \bar{\rho}_e + \bar{\rho}_{Bj} \tag{52}$$

In the 2"-system, this equation reduces to:

$$(\delta_j)_r = r_e + (D_{02}\, D_{i0}\, \hat{D}_{iv}^T - I) r_j \tag{53}$$

where r_j = position of actuator station j in 2"-system, and

$$\hat{D}_{iv} = T_2(\theta_v)\, T_1(\phi_v) \tag{54}$$

For axial actuator stations,

$$r_A = r\begin{bmatrix}0\\1\\0\end{bmatrix}, \quad r_B = r\begin{bmatrix}-\sqrt{3}/2\\-1/2\\0\end{bmatrix}, \quad r_C = r\begin{bmatrix}\sqrt{3}/2\\-1/2\\0\end{bmatrix} \tag{55}$$

For radial stations,

$$r_u = r\begin{bmatrix}-1/\sqrt{2}\\1/\sqrt{2}\\0\end{bmatrix}, \qquad r_v = r\begin{bmatrix}1/\sqrt{2}\\1/\sqrt{2}\\0\end{bmatrix} \tag{56}$$

For roll motor,

$$r_W = r \begin{bmatrix} 0 \\ -1 \\ 0 \end{bmatrix} \tag{57}$$

At axial actuators, only axial centering errors are measured, which are given by the third components of δ_A, δ_B, δ_C. Radial centering errors at stations U and V are obtained by transforming δ_U, δ_V by 45 degrees rotation about the roll axis and then taking appropriate components. Axial and radial centering error at station W are given by third and second components of δ_W.

It is also necessary to compute the time derivatives of centering errors for use in the magnetic actuator models. They are computed along the 2"-system using the method of equation (13).

Magnetic Actuator Models

The radial and axial magnetic actuators, which provide rim suspension forces as well as fine pointing torques, are inherently nonlinear devices. The nonlinearities are present because of the fact that the magnetic force is proportional to current squared, and is inversely proportional to the square of the gap. A bias current technique has been used to remove the current-squared nonlinearity, and a signal proportional to the measured gap is used to multiply each coil current in order to remove the inverse gap squared nonlinearity.

A mathematical model of such a magnetic actuator (axial or radial) was developed by Sperry Flight Systems under contract NAS1-14214. Each actuator model is of order 6 (3 for each of the 2 electromagnets). The model also incorporates limiters and losses due to eddy currents.

Roll Motor Disturbance Model

The roll motor selected for generating tangential force at station W is an ac induction motor with constant fixed field excitation and a control

field excitation which is proportional to the tangential force command. It consists of two curved stator segments, one on the inside and the other on the outside of the rim. The rim is nominally equidistant from both segments. Each segment has a fixed and a control field winding. Since both segments exert attractive forces on the rim which are inversely proportional to the gap squared, each stator winding is made to carry a current which varies linearly with gap in order to achieve radial force balance. A small magnitude anomaly radial force is still present. The roll motor is excited by a 100-Hz carrier--therefore, it is not practical to include a complete roll motor model in view of the enormous computer time requirements. However, a "worst" case situation can be simulated by including a 200-Hz (twice the carrier frequency) sinusoidal radial disturbance force at the roll motor station. A 2- or 3-second time history should then yield adequate results indicating effect of the roll motor.

Cable Forces and Torques

During normal operation, a noncontacting optical data coupler is used for transmission of information between the payload and space shuttle pallet. However, a transmission cable may be used as a backup system for the data coupler. The cable is assumed to be routed through the lateral "coarse" gimbal and the center of payload mounting plate, and is assumed to cause a constant axial force, a constant radial force, a constant torque about the roll axis, as well as axial and radial spring forces (proportional to relative displacements) and a torsion torque (proportional to relative roll angle). This simple representation is used to keep the number of state variables low. In 2"-coordinates, the spring forces acting on the lateral gimbal are given by

$$F_{csi} = K_{si}\, r_{ei} , \quad i = x,y,z \tag{58}$$

The total cable force acting on the lateral gimbal (in 2"-coordinates) is given by

$$F_{ca} = F_{cs} + F_{bias}$$

Relative Euler angles between the payload and the lateral gimbal are computed from:

$$\dot{\alpha}_{vr} = E_{vr}^{-1}\, \Omega_{vr} \tag{59}$$

$$\Omega_{vr} = D_{v_2}\, \omega_v - \omega'_{2_B}$$

where $\alpha_{vr} = (\phi_{vr}, \theta_{vr}, \psi_{vr})^T$ is the attitude of the payload (Euler angles) relative to the lateral gimbal, and E_{vr}^{-1} is the body rate to Euler rate transformation matrix. The cable torque acting on the lateral gimbal is given by:

$$T_{ca} = \begin{bmatrix} 0 \\ 0 \\ \bar{T}_{bias} \end{bmatrix} + \begin{bmatrix} 0 \\ 0 \\ K_{TS}\, \psi_{vr} \end{bmatrix} \tag{60}$$

The cable torque acting on the VA is given by:

$$T_c = D_{2_v}\, T_{ca} \tag{61}$$

where T_c is expressed in the v-system, and D_{2_v} denotes the transformation matrix from the 2- to v-system.

Gimbal Torquer Models

A permanent magnet brushless dc torque motor is used for driving each "coarse" gimbal. It is assumed that the current loop has been compensated to obtain a high bandwidth, so that

$$T_{out} = T_{com} - T_f + T_{cog} + T_{ripple} \tag{62}$$

where T_{out}, T_{com}, T_f are the actual, commanded, and friction torques, and T_{cog} and T_{ripple} are the cogging and ripple torques. Friction torque T_f is generated using a Dahl model (ref. 6)

$$\frac{dT_f}{d\gamma} = \sigma_f \left\{ 1 - \frac{T_f}{T_{fo}} \ \mathrm{Sgn}(\dot{\gamma}) \right\}^i \tag{63}$$

where

γ = gimbal angle (rad)

σ_f = rest stiffness or slope (NM/rad)

T_{fo} = peak or Coulomb friction torque (NM)

i = the friction law (shape of the hysteresis curve).

The friction torque is given by

$$\frac{dT_f}{dt} = \frac{dT_f}{d\gamma} \frac{d\gamma}{dt} \tag{64}$$

Ripple torque is given by:

$$T_{ripple} = p_r \ T_{com} \left(|\sin (f_r \gamma)| - 1 \right) \tag{65}$$

where

p_r = percent of ripple

f_r = ripple frequency = no. of phases × no. of pole pairs.

Cogging torque is given by:

$$T_{cog} = T_{cogo} \sin (f_c \gamma) \tag{66}$$

where

T_{cogo} = peak cogging torque

f_c = cogging frequency = no. of slots.

CONTROL SYSTEMS DESIGN

The two control systems to be designed are the "coarse" gimbal control system and the magnetic suspension and fine pointing control system. The former may use magnetic actuator centering errors, or fine pointing error and rate estimates, or gimbal angle information, depending on the mode of operation. The magnetic suspension control system uses estimates of fine pointing errors and rates, and magnetic actuator centering errors measured by proximity sensors.

"Coarse" Gimbal Control System

For stellar or solar pointing missions, the basic modes of operation of the "coarse" gimbal control system are as follows:

1. Fine-pointing mode, fixed gimbals. In this mode, the "coarse" gimbals are required to be in fixed positions relative to the Shuttle.

2. Fine-pointing with payload following gimbals. In this mode, the gimbals are required to continuously follow the payload in such a manner as to keep the rim properly centered in the magnetic actuators.

3. "Coarse" gimbal backup mode. In this mode, the vernier assembly is mechanically latched to the lateral gimbal, and gimbal command torques are generated using payload attitude and rate estimates.

4. Gimbal slew mode. In this mode, appropriate slew rates are used to drive the gimbals, with the vernier assembly either latched or centered in the magnetic actuators.

The generation of commanded gimbal torquer torques is quite straightforward for mode 1 and mode 3. For the slew mode, the problem lies in computing the desired slew rates. The payload following gimbal control system of mode 2 can be obtained by generating gimbal angle commands which will minimize a norm of the axial and radial centering errors. This is done by linearization about the target pointing angles. The linearized expressions for axial and radial centering errors are

$$\Delta = \begin{bmatrix} \Delta A_z \\ \Delta B_z \\ \Delta C_z \\ \Delta U_r \\ \Delta V_r \end{bmatrix} = \begin{bmatrix} e_3^T \Gamma_1 r_A & e_3^T \Gamma_2 r_A \\ e_3^T \Gamma_1 r_B & e_3^T \Gamma_2 r_B \\ e_3^T \Gamma_1 r_C & e_3^T \Gamma_2 r_C \\ e_2^T T_3' \Gamma_1 r_U & e_2^T T_3' \Gamma_2 r_U \\ e_1^T T_3' \Gamma_1 r_V & e_1^T T_3' \Gamma_2 r_V \end{bmatrix} \begin{bmatrix} \Delta\theta \\ \Delta\phi \end{bmatrix} + d \tag{67}$$

where ΔA_z, ΔB_z, ΔC_z denote incremental axial centering errors at actuator stations A, B, and C, and ΔU_r, ΔV_r denote incremental radial centering errors at actuator stations U and V. $\Delta\theta$, $\Delta\phi$ represent incremental lateral and elevation gimbal angles, and d is a five-dimensional vector.

$$\Gamma_1 = \frac{\partial D_{12}}{\partial \theta} D_{01} D_{io} \hat{D}_{iv}^T \tag{68}$$

$$\Gamma_2 = D_{12} \frac{\partial D_{01}}{\partial \phi} D_{io} \hat{D}_{iv}^T \tag{69}$$

The transformation matrices and their partial derivatives are evaluated at nominal values and target pointing angles. The 5×1 vector d is not a function of $\Delta\theta$ and $\Delta\phi$. Equation (67) can be symbolically written as:

$$\Delta = A_g \beta + d \tag{70}$$

where A_g is a 5×2 matrix, and $\beta = (\Delta\theta, \Delta\phi)^T$. Minimizing the quantity

$$J = ||\Delta||^2 = \Delta^T \Delta \tag{71}$$

with respect to β, the command angle is obtained as:

$$\beta_c = -(A_g^T A_g)^{-1} A_g^T(\Delta - A_g\beta) \tag{72}$$

$$= C_g \Delta + \beta$$

Therefore, the error signal going into the control system is

$$\beta_c - \beta = C_g \Delta \tag{73}$$

where

$$C_g = -(A_g^T A_g)^{-1} A_g^T \tag{74}$$

The gimbal control matrix C_g is dependent on nominal values of pointing angles and requires periodic updating at large intervals of time. Payload following gimbal control can thus be achieved by feedback of five proximity sensor outputs. The desired gimbal torquer torques can be written as:

$$\begin{pmatrix} T_{1_{com}} \\ T_{2_{com}} \end{pmatrix} = -\begin{pmatrix} K_{g_1} & 0 \\ 0 & K_{g_2} \end{pmatrix}\begin{pmatrix} \Delta\dot{\phi} \\ \Delta\dot{\theta} \end{pmatrix} + \begin{pmatrix} L_{g_1} & 0 \\ 0 & L_{g_2} \end{pmatrix} C_g' \Delta \tag{75}$$

where K_{g_i}, L_{g_i} are rate and proportional gains, and C_g' is obtained from C_g by interchanging the two rows. The rate signals in equation (75) can be derived from the proximity sensor outputs using second order networks.

Magnetic Actuator Control System

The magnetic actuator system consists of three axial and two radial actuator stations and one roll motor station. Figure 2 shows the magnetic actuator configuration consisting of three axial actuators spaced 120

degrees apart, two radial actuators spaced 90 degrees apart, and roll motor segments producing a tangential force at one point. The axial actuator stations are labeled A, B, C, and the radial and roll actuator stations are labeled U, V, W. They produce forces F_{ai}, F_{ri}, F_T. The total forces in X_2'', Y_2'', Z_2'' directions produced by the actuator stations on the vernier assembly are

$$\begin{pmatrix} F_x \\ F_y \\ F_z \end{pmatrix} = F = C_F\, f \tag{76}$$

where

$$C_F = \begin{pmatrix} -\frac{1}{\sqrt{2}} & \frac{1}{\sqrt{2}} & 0 & 0 & 0 & 1 \\ \frac{1}{\sqrt{2}} & \frac{1}{\sqrt{2}} & 0 & 0 & 0 & 0 \\ 0 & 0 & 1 & 1 & 1 & 0 \end{pmatrix} \tag{77}$$

and

$$f = (F_{r_1},\ F_{r_2},\ F_{a_1},\ F_{a_2},\ F_{a_3},\ F_T)^T \tag{78}$$

Nominal torques (excluding anomaly torques) produced by these forces on the vernier assembly about the v-system:

$$\begin{pmatrix} M_{vx} \\ M_{vy} \\ M_{vz} \end{pmatrix} = M_v = \zeta_{Av} \times F_A + \zeta_{Bv} \times F_B + \zeta_{Cv} \times F_C + \zeta_{Uv} \times F_U + \zeta_{Vv} \times F_V + \zeta_{Wv} \times F_W \tag{79}$$

where ζ_{jv} is the position of station j in the v-system, and F_j denotes the force vector at the jth actuator station, and so forth. Considering linearized design, the desired response can be obtained by making

$$M_v - C_p(r_{cmv})F = -I_{vo}\,\lambda_{\alpha v} \tag{80}$$

where

$$\lambda_{\alpha v} = (\lambda_{\phi v},\ \lambda_{\theta v},\ \lambda_{\psi v})^T$$

$$\lambda_{\phi v} = 2\rho\omega(\dot{\phi}_v - r_{\phi vc}) + \omega^2(\phi_v - \phi_{vc}) + K_{I\phi v}\,z_{\phi v}$$

$$\dot{z}_{\phi v} = \phi_v - \phi_{vc}$$

(ϕ_{vc}, $r_{\phi vc}$, $K_{I\phi v}$, $z_{\phi v}$ are attitude and rate command, integral gain, and integrator output.) Or

$$C_T\,f - C_p(r_{cmv})C_F\,f = -I_{vo}\,\lambda_{\alpha v} \tag{81}$$

where

$$C_T = r\begin{bmatrix} 0 & 0 & 1 & -\frac{1}{2} & -\frac{1}{2} & 0 \\ 0 & 0 & 0 & \frac{\sqrt{3}}{2} & -\frac{\sqrt{3}}{2} & 0 \\ 0 & 0 & 0 & 0 & 0 & 1 \end{bmatrix} \tag{82}$$

Therefore, desired pointing control can be obtained by making

$$\left(C_T - C_p(r_{cmvo})C_F\right)f = -I_{vo}\,\lambda_{\alpha v} \tag{83}$$

The desired VA translation response can be obtained by making

$$\left(\frac{1}{m_v} + \frac{1}{m}\right) C_F \, f = -\lambda_{re} \tag{84}$$

where λ_{re} is defined similarly to λ_{av}.

Equations (83) and (84) form a system of six linear equations in six unknown components of f. Therefore, the unique solution can be readily obtained by inverting the coefficient matrix.

This design offers complete decoupling of VA rotation and translation, if the VA inertia and c.m. location are accurately known. The commanded magnetic actuator forces are computed in this manner, using proximity sensor outputs, and payload attitude and rate estimates. Magnetic actuator centering error rates are generated from proximity sensor outputs using second order networks. These force commands are fed into the magnetic actuators. In the simulation, the actual output forces are obtained using actuator mathematical models mentioned earlier. Magnetic actuator forces so obtained are in the 2"-system and act at points on the vernier assembly rim. Since the rim is continuous, only the relative roll angle ψ_{rel} of the payload assembly, relative to the lateral gimbal, needs to be considered for obtaining points of application of magnetic forces in v-system. The location of actuator station j in v-system is given by

$$\zeta_{jv} = T_3(\psi_{rel}) \, r_j \tag{85}$$

where r_j is the position of station j in the 2"-system, which is a fixed vector. The three-dimensional actuator force at station j in the 2"-system is

$$F_j = \begin{bmatrix} F_{xj} \\ F_{yj} \\ F_{zj} \end{bmatrix}$$

For example, for station A, $F_{xA} = F_{yA} = 0$, and $F_{zA} = F_{a_1}$, which is the third component of actual magnetic force vector f_o [corresponding to f

of eq. (78)]. For roll motor station W, the radial disturbance force (F_{rd}) can be included in this formulation. The total torque on the payload assembly due to magnetic actuators (in v-system) is given by

$$T_v = \sum_{j=A}^{W} C_p(\zeta_{jv})\, D2_v\, F_j \tag{86}$$

where $D2_v$ is the transformation matrix from 2-system to v-system. The total magnetic actuator force acting on the payload assembly (in v-system) is

$$F_v = D2_v \sum_{j=A}^{W} F_j \tag{87}$$

The expression for T_v in equation (86) is used in the VA rotational equation (44). For the "coarse" assembly, the total reactive force F_r (in 2"-system) acting on the lateral gimbal is

$$F_r = -C_F\, f_o + F_{ca} - e_2\, F_{rd} \tag{88}$$

where f_o denotes the magnetic actuator output force vector corresponding to the command force vector f. The reaction torque on the lateral gimbal is given by

$$T_r = T_{ca} - C_T\, f_o + C_p(r_{cm_2} + r_\ell)\, F_r \tag{89}$$

The torque M_p acting on the complete "coarse" assembly is given by

$$M_p = D_{02}^T \left[C_p(D_{02}\, \rho_1' + D_{12}\, r_d + r_{cm_2} + r_\ell)\, F_r + T_{ca} - C_T\, f_o \right] + T_{RCJ} + T_d \tag{90}$$

in the O-system, where T_{RCJ} and T_d denote reaction control jet torque and disturbance torque.

These expressions for F_r, T_r, and M_p are used in the "coarse" assembly equations of motion, equations (19), (29), and (36).

SENSOR MODELS

Attitude of the shuttle is controlled by vernier reaction control jets. In the simulation, however, only one thruster firing is included in order to simulate the "worst case" reaction control jet transient. Therefore, the shuttle attitude measurement system is not necessary for the simulation. "Coarse" gimbal positions are measured by sine-cosine resolvers. Axial and radial centering errors at the corresponding magnetic actuator stations and at the roll motor station are measured by noncontacting proximity sensors. Outputs of the proximity sensors are assumed to be contaminated with Gaussian zero-mean white noise. The payload attitude and rate measurement system consists of three rate gyros and sun sensors/star trackers. The gyros are assumed to be low noise, dry-tuned types, and sun sensors are assumed to be high-resolution, monochromatic light type. Three rate and attitude error measurements (one per axis) are assumed to be available for feeding into the fine-pointing control system. Figure 4 shows a single axis block diagram of the payload attitude and rate measurement system. Each gyro output is contaminated with a zero-mean colored noise and a Wiener process bias. The sun sensor outputs, which are discrete-time, are contaminated with zero-mean white noise which represents electronics noise, thermal (shot) noise, and quantization error. A bias may also be present in the sun sensor. Gyro drift rate, sun sensor bias, and sun sensor boresight misalignment are important sources of low-frequency error. Gyro drift rate can be either compensated for or estimated by a state estimator which gives an asymptotically unbiased rate estimate. Sun sensor bias errors are usually measureable and repeatable, and can be compensated to a large extent by the sun sensor electronics. Any uncompensated sun sensor bias or misalignment will affect the mean pointing error (pointing "accuracy"), and not the RMS pointing error (pointing "stability"). The accuracy requirements are usually far less stringent than the stability requirements. Therefore, small sun sensor bias errors can be tolerated, and are assumed to be absent. Single-speed

wound rotor resolvers are included in the "coarse" gimbal assembly for position readout and control of the gimbal angles. A roll axis resolver is used to measure payload roll angle relative to the lateral gimbal.

PAYLOAD ATTITUDE STATE ESTIMATORS

Pointing performance of the ASPS, or any other pointing system, depends on the payload attitude and rate signals used in the synthesis of the control torque. If no estimator is used, it can be shown (ref. 4) that the pointing performance of a completely isolated assembly is severely limited. In fact, the pointing error in this case increases directly with controller bandwidth, reciprocal of damping ratio, and measurement noise level. Reference 8 contains a detailed treatment of the estimator design problem. Two types of estimators have been considered in reference 7, which give attitude estimates and asymptotically unbiased rate estimates despite gyro bias. The first type does not utilize the input (control) torque information, while the second type of estimator utilizes the input torque information in its prediction model. In the case of ASPS, the input torque can be accurately measured. However, performance of the second type of estimator (Filter 3) is critically dependent on the input noise level, which was not accurately known at the time of writing this report. Therefore, the first type of estimator (Filter 1A), one for each axis, has been included in the present simulation. These estimators generate estimates $\hat{\phi}_v$, $\hat{\theta}_v$, $\hat{\psi}_v$, $\dot{\hat{\phi}}_v$, $\dot{\hat{\theta}}_v$, $\dot{\hat{\psi}}_v$ for use in the fine pointing control loop.

SIMULATION DESCRIPTION

The mathematical model of ASPS/Space Shuttle system consists of a set of nonlinear ordinary differential equations. The nonlinearities include all trigonometric nonlinearities, magnetic actuator nonlinearities, gimbal and gimbal torquer nonlinearities, etc. The control systems consist of a magnetic actuator control system, "coarse" gimbal control system, and a space shuttle attitude control system. The magnetic actuator control system blends the discrete-time signal $\lambda_{\alpha v}$ [eq. (83)] generated

using payload attitude and rate estimates, with the continuous signal λ_{re} [eq. (84)] to synthesize the magneti actuator command-force vector. (The signal λ_{av} is generated every T_{fil} seconds and kept constant for T_{fil} seconds, where T_{fil} is the estimator update interval.) Although this control scheme has been assumed in the present simulation, other schemes such as multirate sampling (different sampling rates for attitude and rate feedback) may also be suitable for ASPS application. However, results of investigation of these schemes were not available at the time of writing this report. Therefore, the single-rate sampling scheme mentioned above has been used in the simulation.

The "coarse" gimbal control system is continuous time, except when used in the backup gimbal pointing mode. In that case, the control scheme would be similar to the fine-pointing control scheme discussed above.

The space shuttle attitude is controlled by vernier reaction control jets. However, for computing RMS pointing errors, a low bandwidth control system using an annular momentum control device (AMCD) or control-moment-gyros (CMG's) has been assumed for the space shuttle. This assumption is not restrictive (ref. 4) because, in the case of ASPS, the payload assembly is almost completely isolated from the shuttle. However, for computing peak pointing errors for the "worst case" reaction control jet transient, a control jet force pulse of -222.4 N in the Z_o direction is applied, producing a disturbance torque of -2487.9 N-m about the X_o axis. The duration of the pulse is 0.52 seconds, and occurs when the shuttle angular velocity about the X_o axis is 0.00435 degree/second.

It was found that the ac resistance in the magnetic actuator model could be ignored without significant effects, reducing the order of each (axial and radial) actuator from 6 to 4. Various options are available in the computer program. These options include: inclusion or exclusion of payload attitude state estimators in the loop; use of magnetic actuators or latched vernier assembly backup mode; inclusion or exclusion of attitude measurement noise; proximity sensor noise; worst case shuttle vernier jet transient; roll motor radial disturbance force; choice of payload following or fixed gimbal modes; etc. Dimension of the state vector (excluding state estimators) is 65 for normal operation and 30

for the backup pointing mode. In order to keep the number of state variables low, gimbal angular rates and centering error rates are assumed to be available for control synthesis, instead of generating them using second-order networks.

Table 1 lists the noise sources acting on the system, and their standard deviations. All noises are assumed to be white and Gaussian. All the noise processes, except the sun sensor noise, are continuous time. For digital simulation, however, they must be represented by discrete pulses. This can be approximately done by choosing an integration interval $T_i \leq T_{fil}$, and generating random numbers with standard deviations given by continuous standard deviations divided by $\sqrt{T_i}$. The random numbers generated are held constant in each interval T_i. This sequence of random amplitude pulses has approximately the same power as the continuous white noise. In the present simulation, T_i and T_{fil} were both 0.01 sec. The simulation proceeds in the following manner: the differential equations are solved for T_i seconds until time increment T_{fil} is reached (the ratio T_{fil}/T_i is an integer greater than or equal to 1); new state estimates and vernier torque commands are generated and held constant for the next T_{fil} seconds (magnetic actuator force commands are continuously generated using vernier torque commands and continuous proximity sensor outputs); the differential equations are solved again for T_i seconds, and so forth. All noise processes are generated every T_i seconds, except the sun sensor noise, which is generated every T_{fil} seconds.

Mean and RMS errors are computed by solving the differential equations until the statistics have evolved, and then computing means and standard deviations of the pointing errors as the solution continues. Sensitivities to various noise sources are computed by making all except the corresponding standard deviation zero. Two options were included in the computer program for solving the differential equations--Euler integration and fifth-order Adams method. The latter was found to perform satisfactorily for all cases because of its ability to solve stiff differential equations. The former may be useful for simpler cases (such as backup "gimbal pointing systems").

NUMERICAL RESULTS AND DISCUSSION

In order to evaluate the performance of ASPS, a 3.7-m long, 66-cm diameter cylindrical payload having a mass of 270 kg was selected. This payload is well within the limits of the present magnetic actuators and is one of the two payloads used in reference 3. Table 2 gives the parameters of the space shuttle orbiter. "Coarse" gimbal torquer and friction parameters are given in tables 3 and 4, and cable parameters are given in table 5. Payload assembly parameters are given in table 6. Table 7 describes the control system modes and parameters used. Table 1 gives a list of noise sources and their nominal standard deviations.

In order to evaluate ASPS performance, it is necessary to include the errors made in measurement of VA c.m. location and inertia matrix, since the measured quantities are used in control systems design. An error of -1 percent was assumed in the measurement of r_{cmv}, and of the VA inertia matrix I_v in all the computer runs. The target pointing angles are assumed to be $\phi = 45°$, $\theta = 45°$, $\psi = 0°$, which form one of the worst combinations (ref. 4). The basic computer runs for evaluationg ASPS performance are described below:

1. Response to initial condition offsets.
2. Peak pointing errors for the worst case vernier reaction control jet (VRCJ) disturbance.
3. RMS error computation.
4. Sensitivities of pointing errors to various noise sources.

These computer runs are repeated with the following changes:

a. Use of backup gimbal pointing system (with payload assembly latched to lateral gimbal).

b. No estimators used.

c. Cable used for data transmission.

d. "Coarse" gimbals not in the payload following mode.

That is, the gimbal servos hold them in their nominal positions.

Response to an initial condition offset of 20 arcseconds in VA attitude and 2 mm (for each axis) in VA translation is shown in figure 5. Although a 2.5-arcsecond undershoot occurs, the transient dies down in about 1.5 sec. The magnetic actuator centering errors decay much more slowly due to low suspension bandwidth.

The worst-case VRCJ transient was next simulated, as described earlier. Table 8 shows peak pointing errors under different conditions. Peak pointing error was 0.00875 arcsecond (in ϕ_v) in the absence of noise, and 0.01006 arcsecond when noise was present. When the cable was used for data transmission, the peak error increased to 0.0236 arcsecond. Figure 6 shows typical pointing error and centering errors for this transient when the cable was used. All peak centering errors were below 4 mm for all these cases. These results were obtained for a magnetic actuator current-loop bandwidth of 300 Hz. It was found that variation of current loop bandwidth had significant effect on peak pointing errors. Figure 7 shows the variation of peak pointing errors with current loop bandwidth.

Theoretically, peak pointing errors should be zero in the absence of noise and errors in measuring I_v and r_{cmv}. However, in reality, the peak pointing error is never zero because of (1) a change in VA roll position due to the transient, causing a change in the location of the vernier assembly c.m. with respect to magnetic actuators, (2) magnetic actuator nonlinearity, that is, error between commanded and actual forces, (3) finite bandwidth of magnetic actuator current loop, and (4) sampling of commanded magnetic actuator torques.

The results described above were obtained using the "payload following" gimbal mode. Fixed gimbal mode was next simulated in which the gimbals are held by the control system in a fixed position relative to the shuttle. In this case, it was found necessary to increase the bandwidth of the VA translation control system to 0.13 rad/sec in order to limit the magnetic actuator centering error excursions. This resulted in somewhat larger (about 15 percent higher) peak pointing errors as shown in table 8. This demonstrated the advantage of the payload following mode.

Peak pointing errors during the backup gimbal pointing mode (with VA latched to lateral gimbal) with noise and estimators present, are also

given in table 8. The largest peak error for this mode is 1.618 arcseconds in θ_V-axis, which represents almost a factor of 400 deterioration compared to the "normal operation" case. Figure 8 shows the response of the backup system to the worst-case VRCJ transient.

Root-mean-squared (RMS) pointing errors were next obtained as described in the preceding section, for various cases. Table 9 shows the results for normal operation and for the backup mode. The most significant source of error is proximity sensor noise. Contribution of the attitude measurement system noise is very small (for the nominal standard deviations). In order to investigate the effect of larger attitude measurement noise, the sun sensor noise standard deviation was varied from its nominal value, up to 2000 times the nominal value, and the RMS pointing errors were obtained. Figure 9 shows the resulting variation of RMS pointing errors. When the cable was used, the RMS pointing error increased only slightly (table 9) although the peak error for the worst case VRCJ transient almost doubled.

In order to investigate the effect of roll motor anomaly torque, a sinusoidal radial force with a peak of 0.0622 N and a frequency of 200 Hz (twice the carrier frequency) was applied at the roll motor station W. As discussed earlier, because of the high frequency, a 5-sec time response was computed for investigating this effect. All other noise sources were held at zero. The resulting RMS pointing errors were (1.12, 0.231, 0.275) $\times$ 10^{-4} arcsecond for ϕ_V, θ_V, and ψ_V, respectively, which are insignificant compared to the effect of proximity sensor noise.

CONCLUSIONS

A detailed nonlinear mathematical model was developed for the ASPS/Space Shuttle system. All trigonometric nonlinearities as well as nonlinearities in various components such as magnetic actuators, "coarse" gimbals, and torquers were incorporated. Control laws and payload attitude state estimators were designed for solar/stellar pointing missions. A computer program was developed to simulate the system, and the pointing performance was evaluated for various conditions for normal operation and for the backup

"gimbal pointing" mode. The RMS errors for normal operation were (0.9949, 1.007, 2.844) $\times 10^{-3}$ arcsecond for the three axes, and were 0.05359 and 0.05731 arcsecond in pitch and yaw axes for the backup pointing mode. The most significant source of error for the noise parameters considered was the proximity sensor noise. Peak pointing errors for the worst case vernier reaction control jet transient were 0.00301, 0.00398, and 0.0101 arcsecond for normal operation and 1.485 and 1.618 arcseconds for the backup mode. Use of a cable for data transmission under normal operation was found to cause about a 100 percent increase in peak pointing errors, but minimal increases in RMS errors. It can be concluded on the basis of these results that ASPS can provide very high quality pointing performance in the presence of sensor and actuator noise and disturbances.

REFERENCES

1. Anderson, Willard W.; and Groom, Nelson J.: The Annular Momentum Control Device (AMCD) and Potential Applications. NASA TN D-7866, March 1975.

2. Anderson, Willard W.; and Joshi, Suresh M.: The Annular Suspension and Pointing (ASP) System for Space Experiments and Predicted Pointing Accuracies. NASA TR R-448, 1975.

3. Joshi, Suresh M.: Analysis of a Magnetically Suspended High Performance Instrument Pointing System. AIAA Journal of Guidance and Control, Vol. 1, No. 2, March/April 1978.

4. Joshi, Suresh M.: Linear Analysis and Pointing Performance Prediction of ASPS/Space Shuttle System. NASA CR-149033, 1976.

5. Greenwood, Donald T.: Principles of Dynamics. Prentice-Hall, 1965.

6. Anonymous: Space Shuttle Experiment Pointing Mount (EPM) Systems: An Evaluation of Concepts and Technologies. Jet Propulsion Laboratory Report No. 701-1, April 1, 1977.

7. Joshi, Suresh M.: On Attitude Estimation Schemes for Fine Pointing Control. IEEE Trans. Aerospace and Electronic Systems, Vol. AES-14, No. 2, March 1978.

BLANK PAGE

Table 1. Measurement noise parameters (nominal).

	Number of Measurements Used	Standard Deviation
Proximity sensor	5	4.82×10^{-8} m
Sun sensor noise, n_s	3	0.00283* arcsec
Rate gyro (rate) noise, v	3	1.632×10^{-6} arcsec/sec
Rate gyro (bias) noise, n_u	3	1.025×10^{-8} arcsec/sec

* Discrete time.

le 1. Measurement noise parameters (nominal).

Number of Measurements Used	Standard Deviation
5	4.82×10^{-8} m
3	0.00283* arcsec
3	1.632×10^{-6} arcsec/sec
3	1.025×10^{-8} arcsec/sec^2

Table 2. Parameters of Space Shuttle Orbiter.

Mass, kg	86176.2
Inertias, kg-m^2	
I_{xx}	7,882,725
I_{yy}	1,037,200
I_{zz}	8,082,030
I_{xy}	6,779
I_{xz}	2,711
I_{yz}	-178,968

Crew station location in (X_o, Y_o, Z_o) system, m...(0, -16.002, 0.594)

Location of point P_e in (X_o, Y_o, Z_o) system, m...(0, 2.2, 0.75)

Table 3. "Coarse" gimbal parameters.

	Elevation Gimbal	Lateral Gimbal
Mass, kg	31.1	103.5
Inertias (x,y,z), kg-m^2	0.575, 0.575, 0.228	3.84, 3.84, 6.5
Center of lateral gimbal axis in 1'-system (r_d), m	(0, 0, 0.21)	
Location of lateral gimbal center O in 2'-system, relative to lateral gimbal c.m. (r_ℓ), m	(0, 0, 0.027)	
Location of lateral gimbal c.m. in 2'-system (r_{cm_2}), m	(0, 0, 0.208)	
Location of elevation gimbal c.m. in 1'-system (r_{cm_1}), m	(0, 0, 0.1)	

Table 4. Gimbal torquer and friction parameters.

Rest stiffness (σ_f), N-m/rad	6.77
Peak or Coulomb friction torque (T_{f_o}), N-m	0.0316
Percent ripple (p_r)	2
Ripple frequency (f_r), Hz	48
Cogging frequency (f_c), Hz	96
Peak cogging torque (T_{cogo}), N-m	0.16

Table 5. Cable parameters.

Cable translation spring constants (radial, axial), N/m	1.05, 0.35
Cable bias forces (radial, axial), N	0.01405, 0.00445
Cable torsional spring constant (Z), N-m/rad	0.005
Cable bias torque (Z), N-m	0.001

Table 6. Payload (vernier) assembly parameters.

Mass , kg	270
Inertias (x,y,z), kg-m^2	319, 319, 15
Location of c.m. in v-system (x,y,z), m	0.07, 0.07, 1.83
Radius of PMP, m	0.365

Table 7. Control system parameters.

	Type of Control	Damping ratio, ρ	Natural Frequency, ω Nominal	Natural Frequency, ω Range	Nominal Location of Root due to Integrator
"Coarse" gimbals	Proportional and Derivative	0.7	7.5 Hz	3 - 10 Hz	
Payload attitude	Proportional-Integral-Derivative (PID)	0.7	1 Hz	1 - 4 Hz	1 rad/sec
Payload assembly translation	Proportional-Integral-Derivative (PID)	0.7	0.1 rad/sec	0.05 - 0.3 rad/sec	0.1 rad/sec
"Coarse" gimbals in backup pointing mode	Proportional-Integral-Derivative (PID)	0.7	1 Hz	1 - 3 Hz	1 rad/sec

Table 8. Peak pointing error.

		Peak pointing error, arcsecond ϕ_v	θ_v	ψ_v
Normal Operation	No noise present	0.00256	0.00363	0.00875
	Noise and estimator present	0.00301	0.00398	0.0101
	Noise, estimator, and cable present	0.00758	0.00707	0.0236
	Noise and estimator present, "payload following" mode not used	0.00334	0.00453	0.0116
Backup Mode (VA latched)	Noise and estimator present	1.485	1.618	

Table 9. RMS pointing errors.

	Case	Pointing error, a	
		ϕ_v	θ_v
Normal Operation	Attitude measurement noise only	0.7978×10^{-4}	1.329×10^{-4}
	Proximity sensor noise only	0.9818×10^{-3}	1.004×10^{-3}
	All noise present but no estimator	1.001×10^{-3}	1.008×10^{-3}
	All noise and estimator present	0.9949×10^{-3}	1.007×10^{-3}
	All noise, estimator, and cable present	1.031×10^{-3}	1.034×10^{-3}
Backup Mode (VA latched)	All noise and estimator present	0.05359	0.05731

Table 9. RMS pointing errors.

Case	Pointing error, arcsecond		
	ϕ_v	θ_v	ψ_v
asurement noise	0.7978×10^{-4}	1.329×10^{-4}	0.5375×10^{-4}
ensor noise only	0.9818×10^{-3}	1.004×10^{-3}	2.835×10^{-3}
resent but no	1.001×10^{-3}	1.008×10^{-3}	2.850×10^{-3}
nd estimator	0.9949×10^{-3}	1.007×10^{-3}	2.844×10^{-3}
estimator, and nt	1.031×10^{-3}	1.034×10^{-3}	2.922×10^{-3}
nd estimator	0.05359	0.05731	

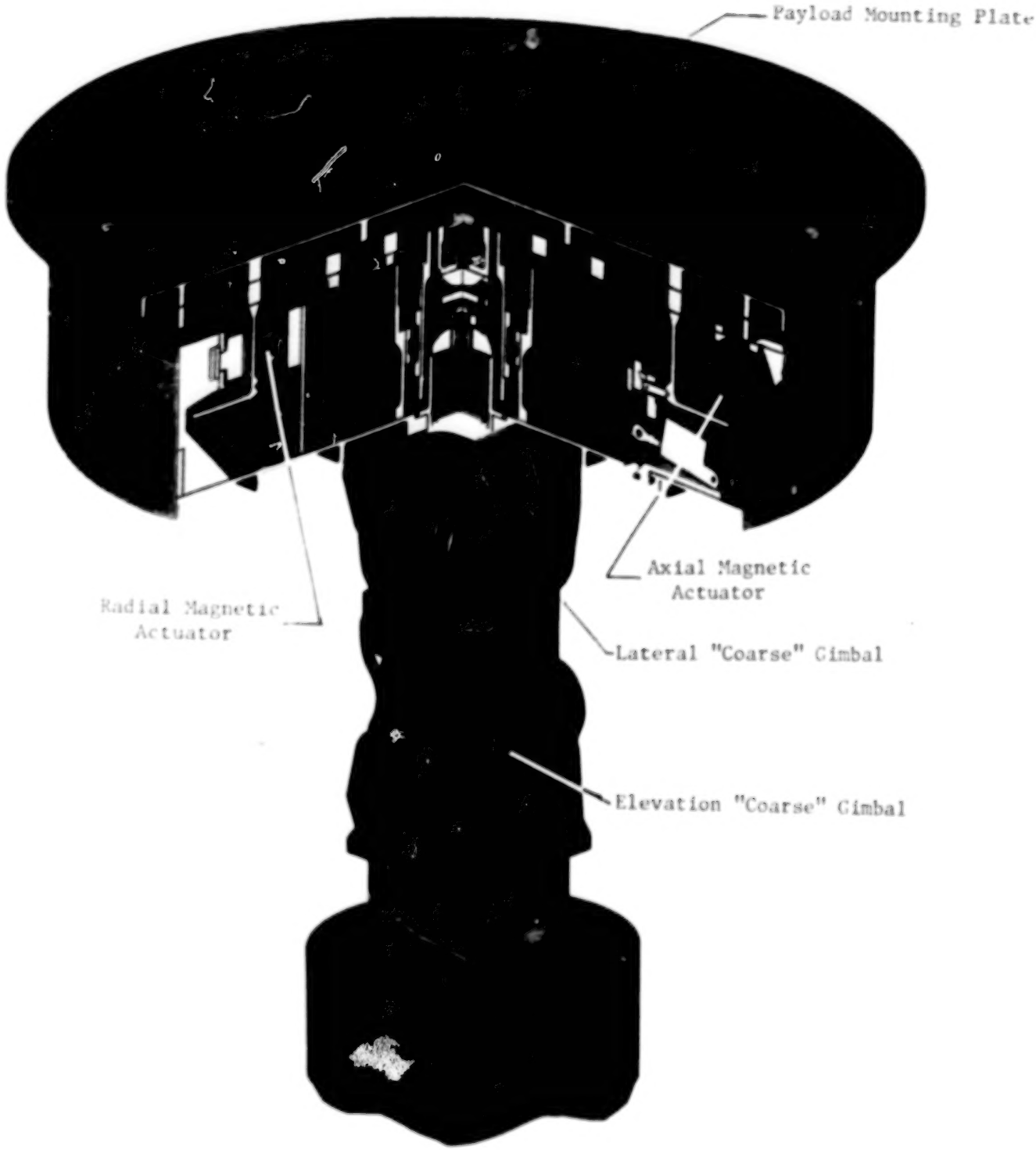

Figure 1. Annular Suspension and Pointing System (ASPS).

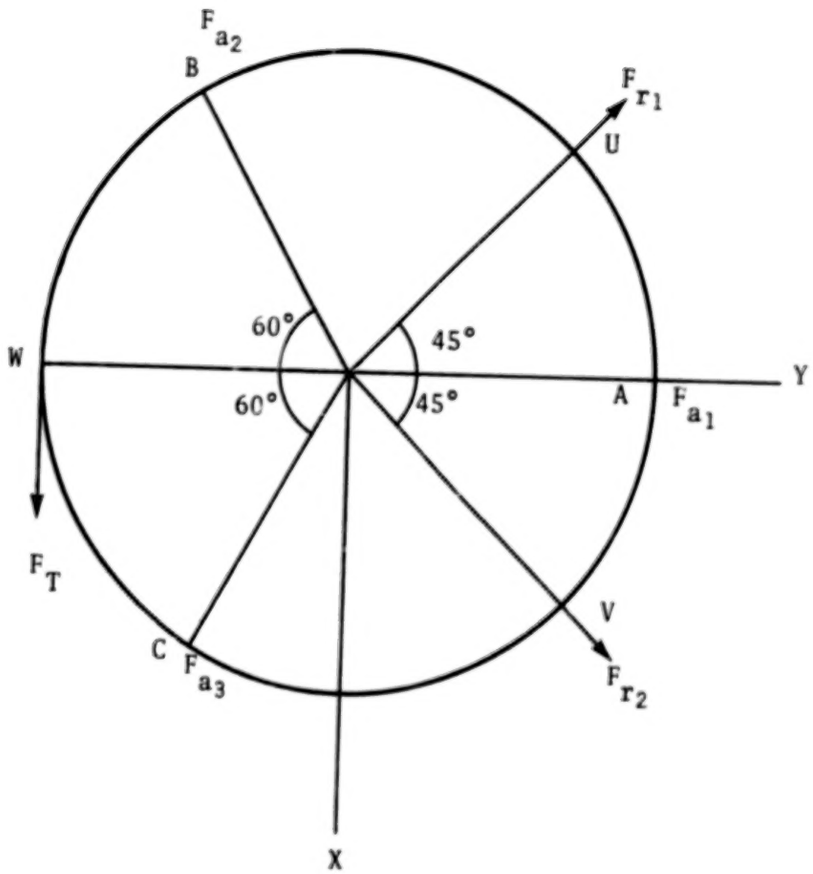

Figure 2. Magnetic actuator configuration.

Figure 3. Definition of position vector

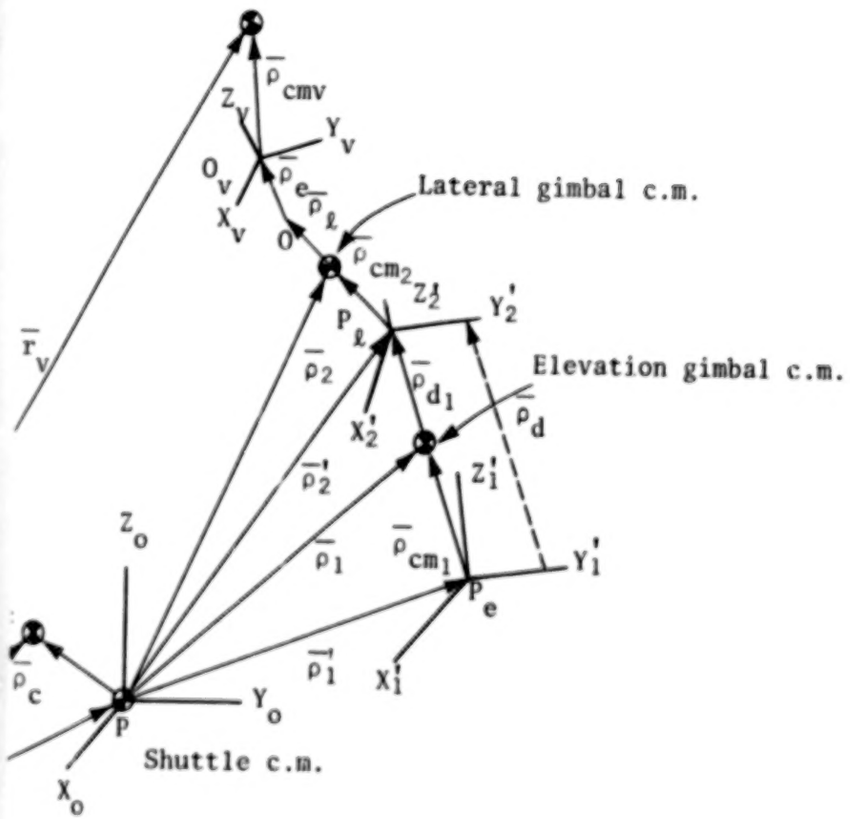

3. Definition of position vectors.

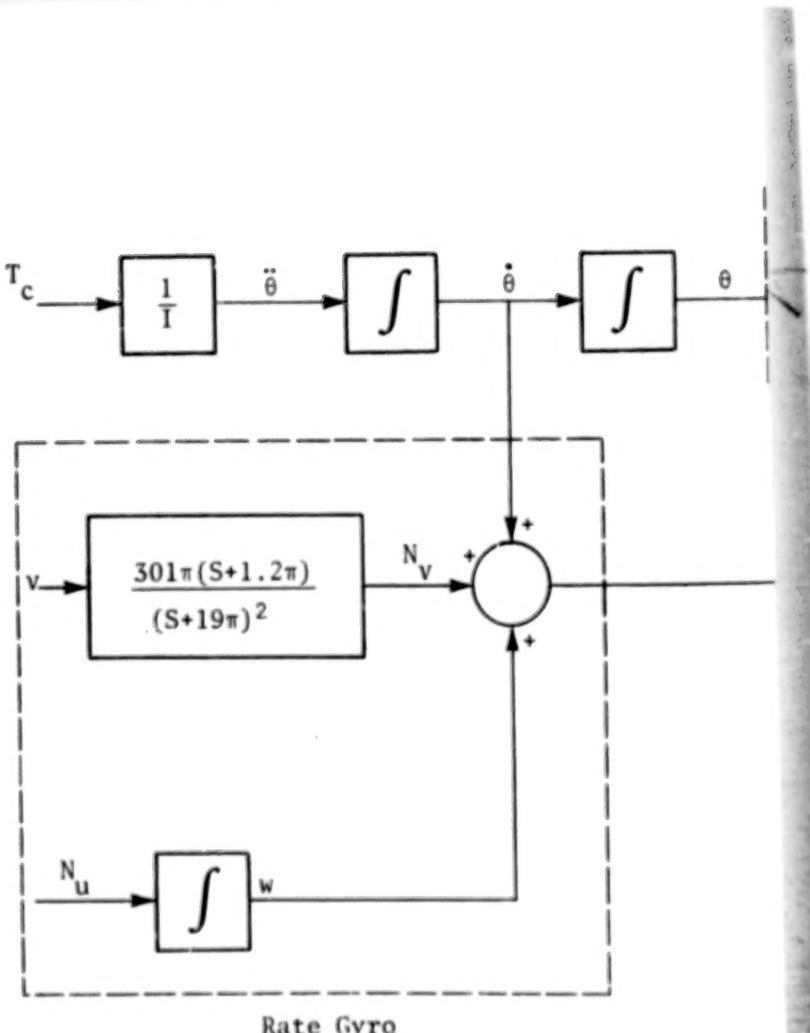

Figure 4. Payload attitude measurement

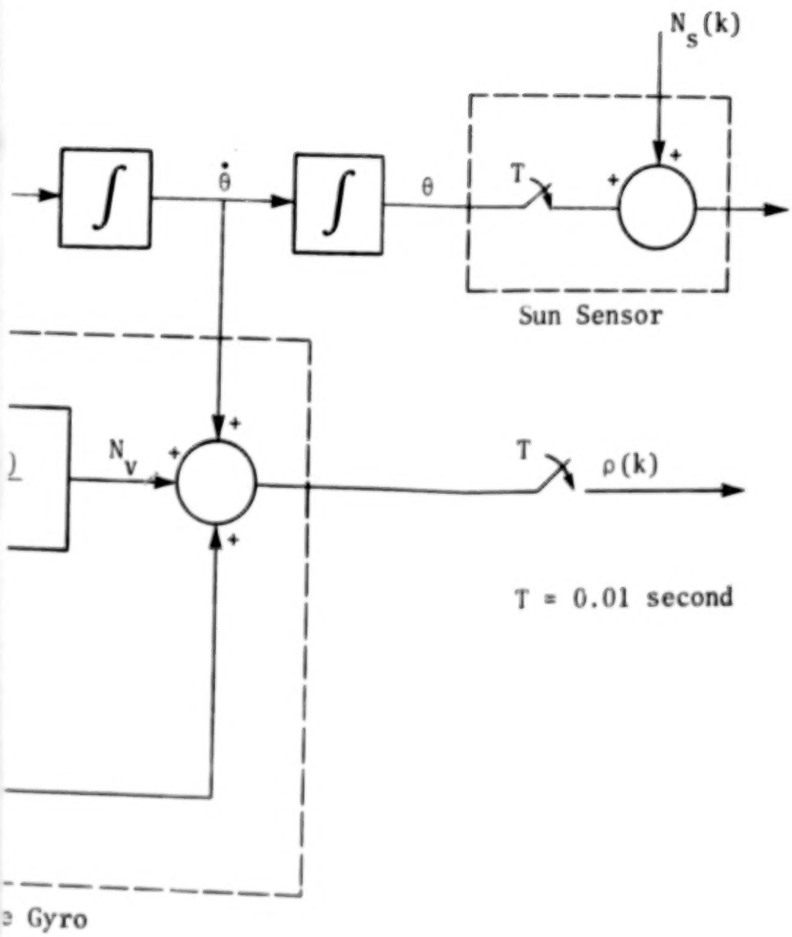

Payload attitude measurement system.

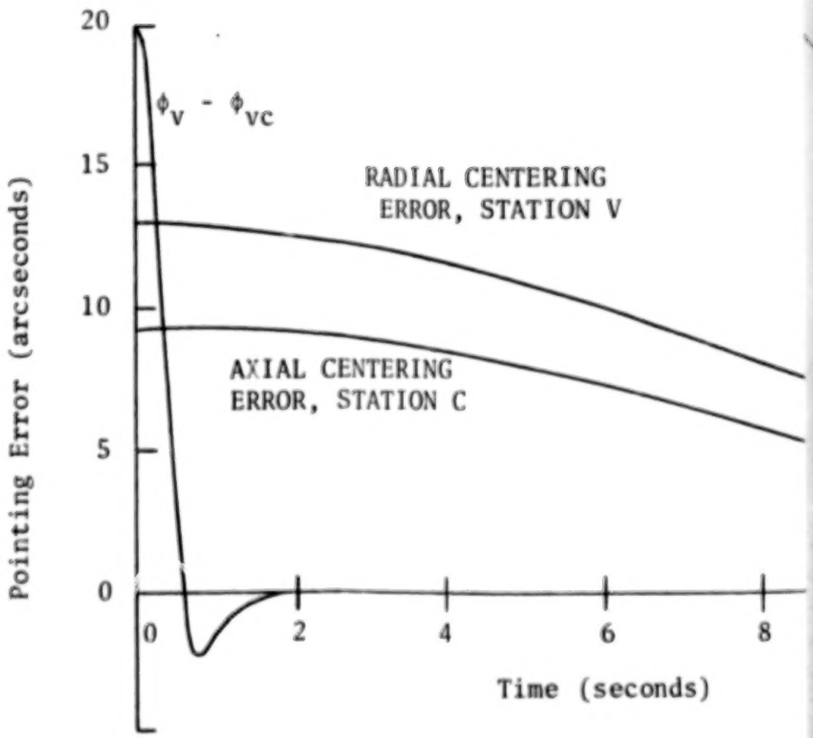

Figure 5. Response to initial condition o

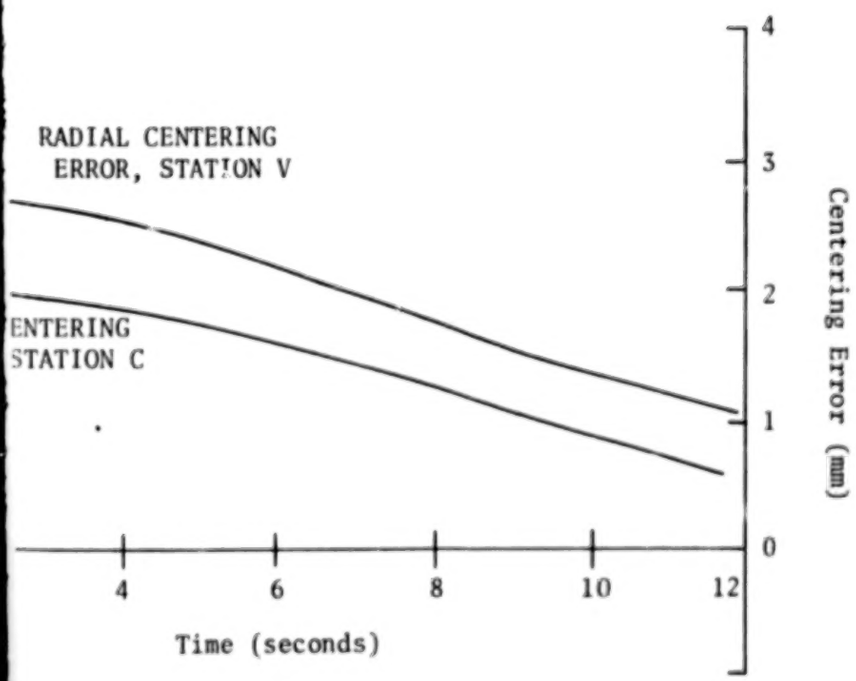

Response to initial condition offset.

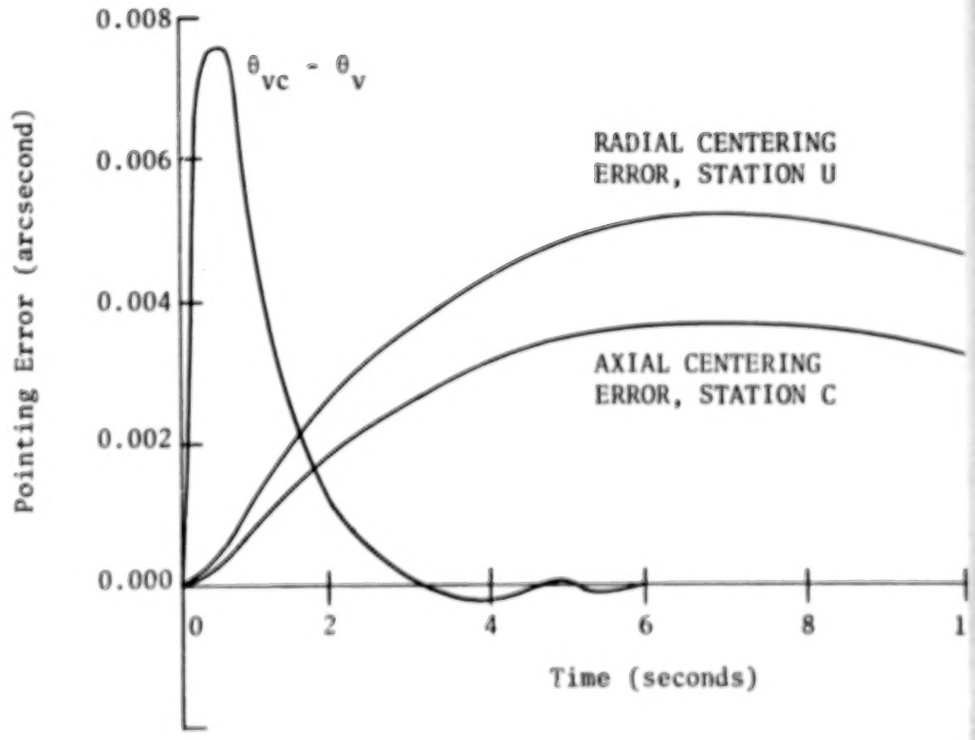

Figure 6. Response to worst case VRCJ disturbance (with

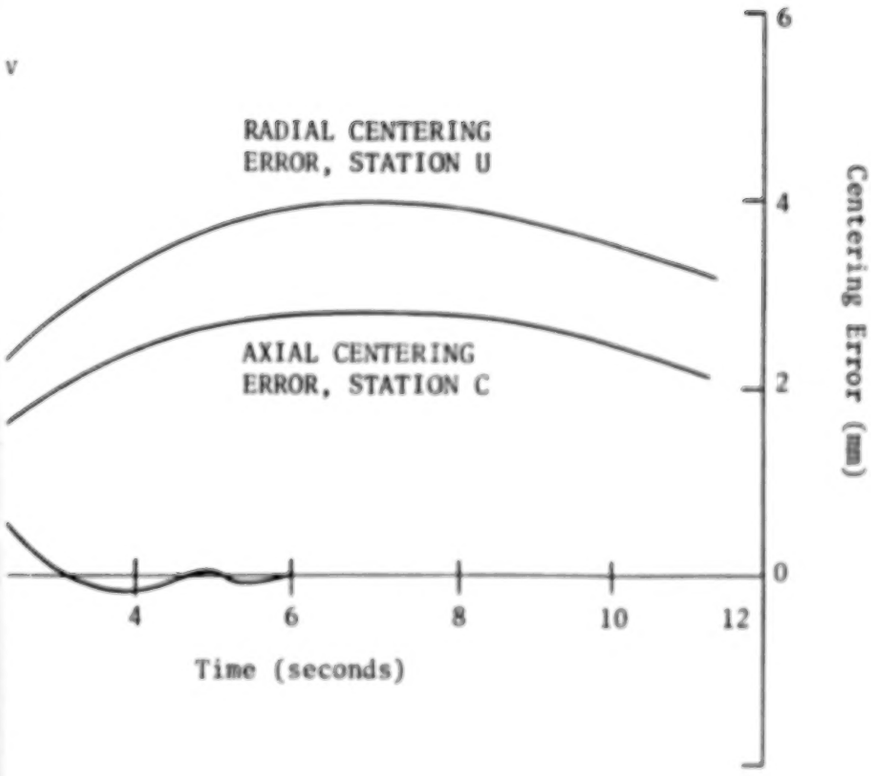

nse to worst case VRCJ disturbance (with cable).

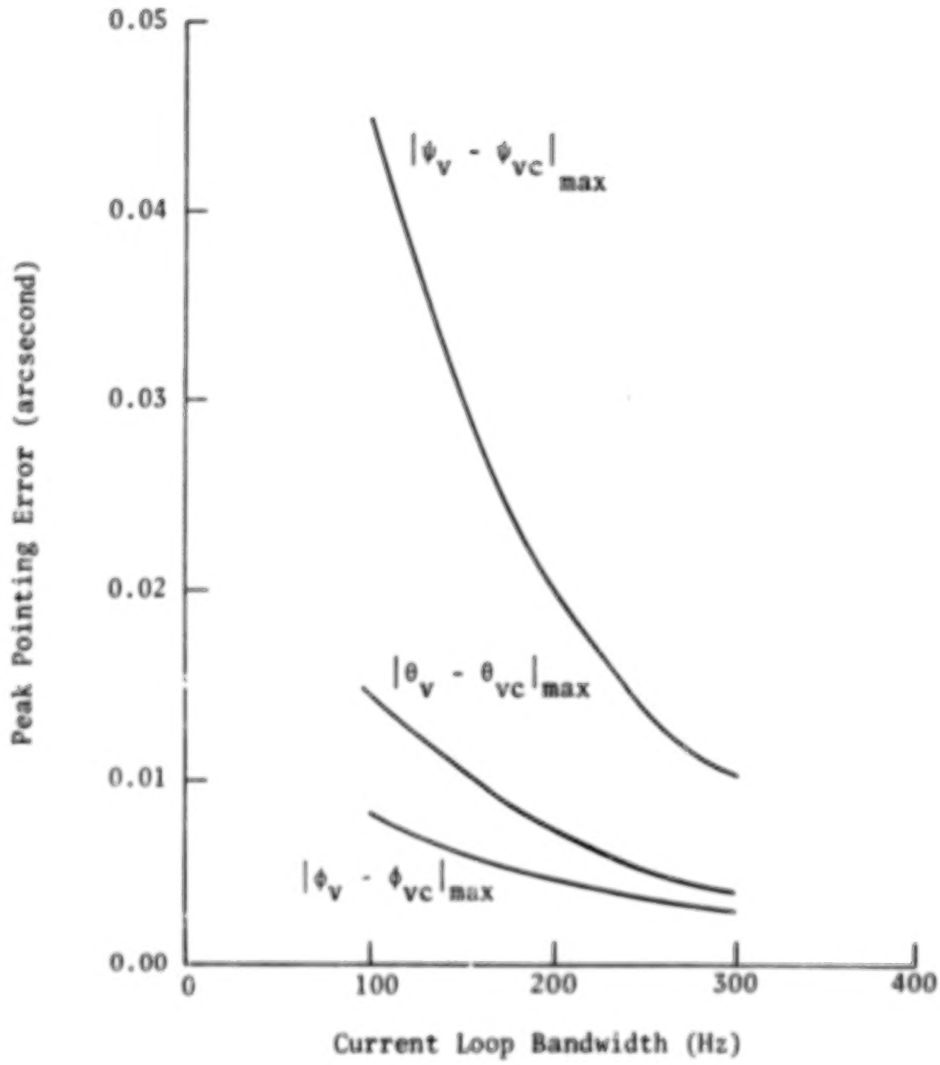

Figure 7. Effect of magnetic actuator current loop bandwidth on peak pointing errors.

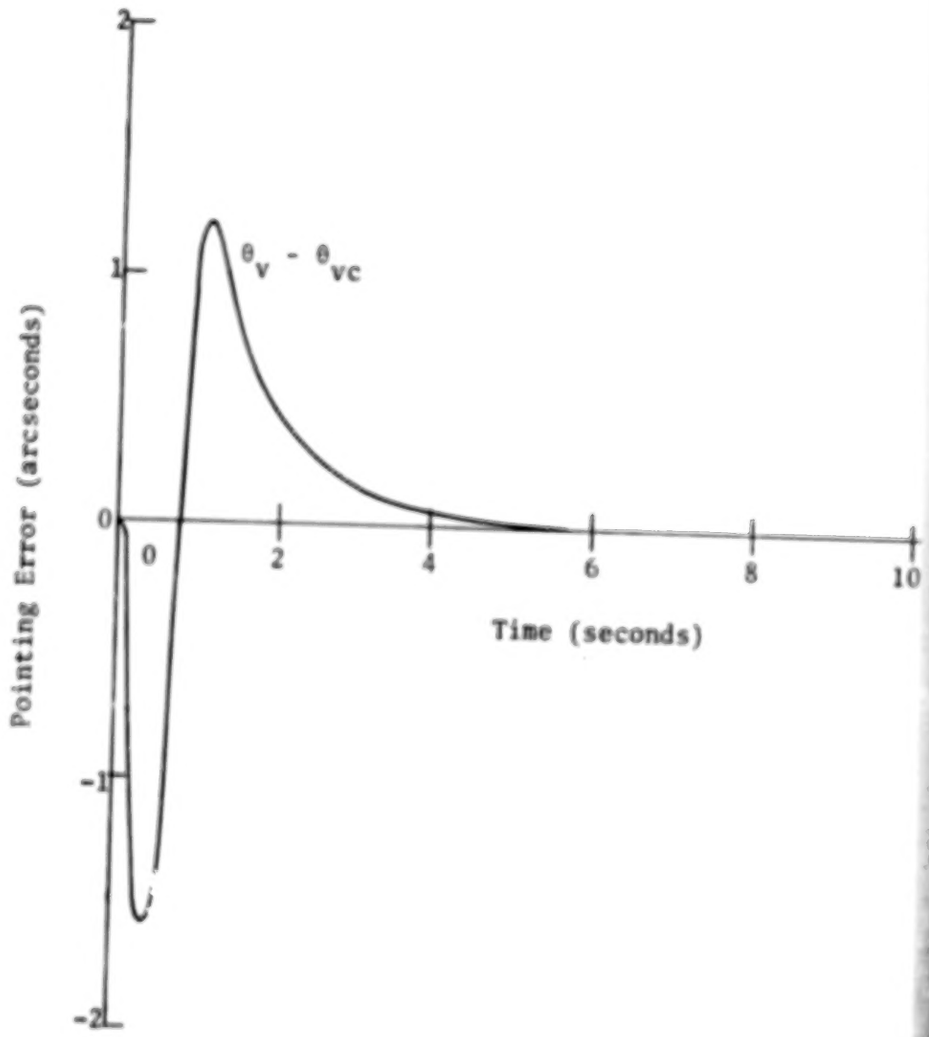

Figure 8. Response of backup system to worst-case VRCJ transi

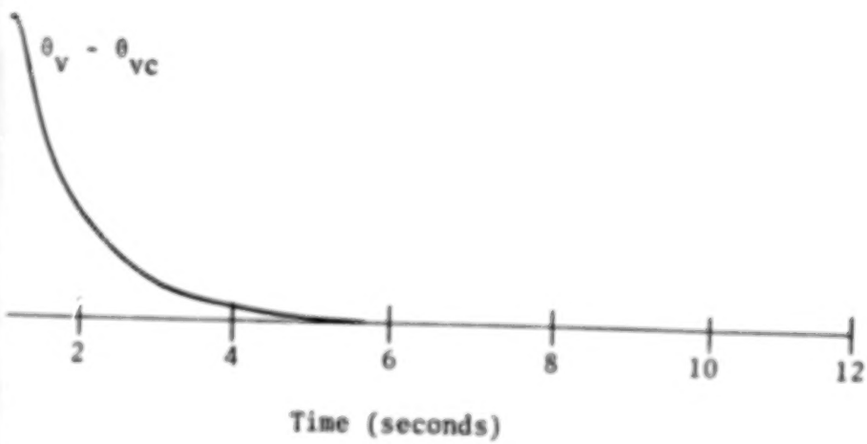

onse of backup system to worst-case VRCJ transient.

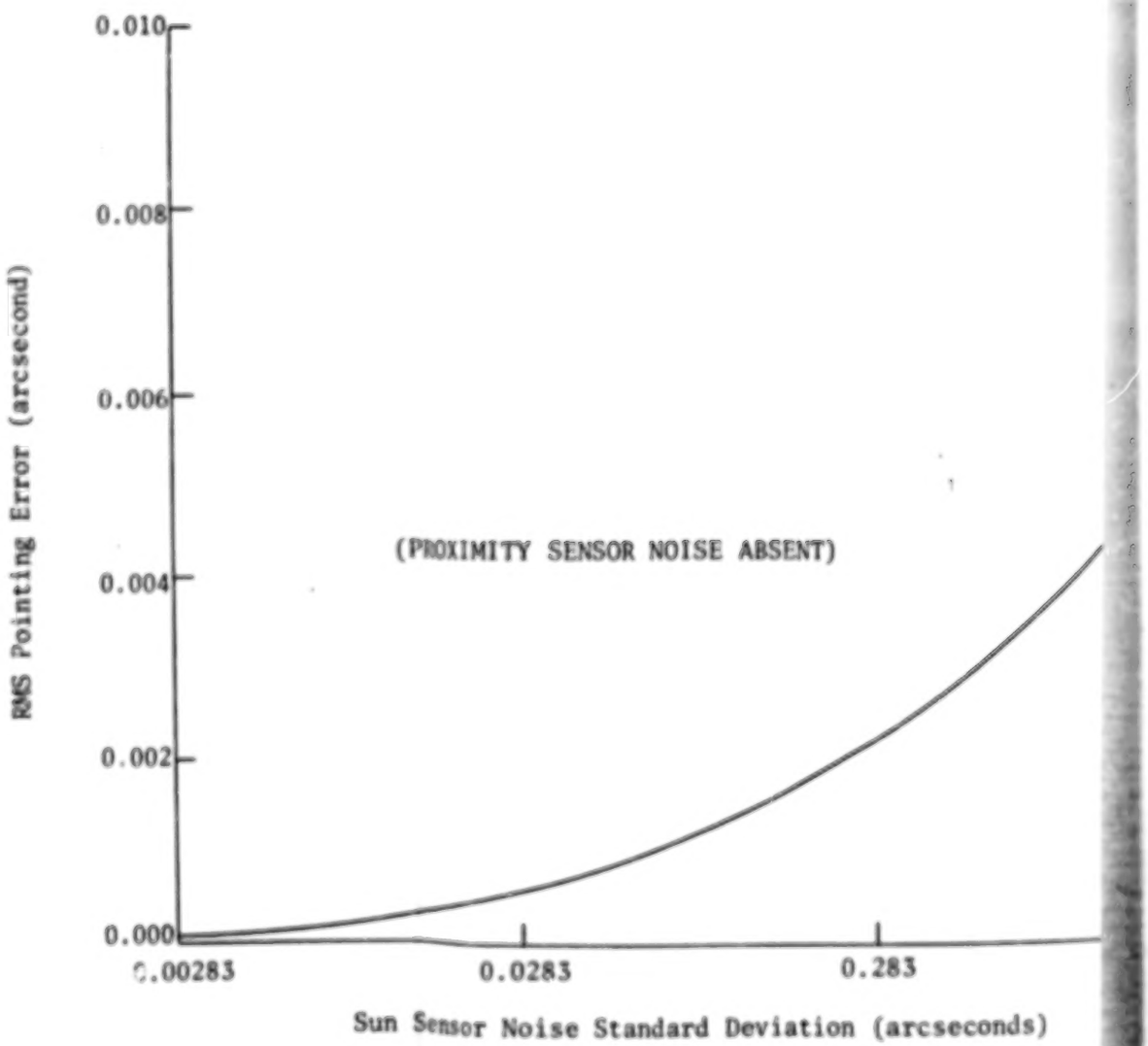

Figure 9. Variation of RMS errors with sun sensor noise level

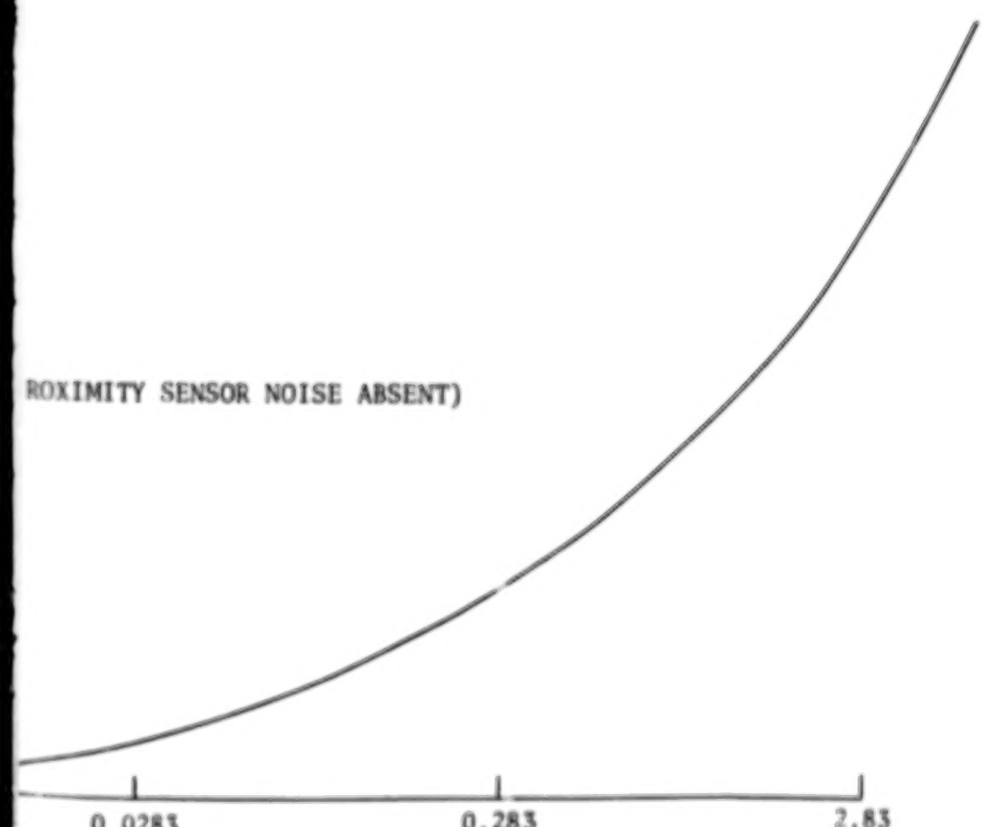

ensor Noise Standard Deviation (arcseconds)

iation of RMS errors with sun sensor noise level.

1. Report No.	2. Government Accession No.	3. Recipient's Catalog No.
NASA CR-3040		

4. Title and Subtitle	5. Report Date
Nonlinear Analysis and Performance Evaluation of the Annular Suspension and Pointing System (ASPS)	August 1978
	6. Performing Organization Code
7. Author(s)	8. Performing Organization Report No.
Suresh M. Joshi	
9. Performing Organization Name and Address	10. Work Unit No.
Old Dominion University Research Foundation Norfolk, Virginia 23508	506-19-13-03
	11. Contract or Grant No.
	NSG 1241
	13. Type of Report and Period Covered
12. Sponsoring Agency Name and Address	Contractor Report
National Aeronautics and Space Administration Washington, DC 20546	14. Sponsoring Agency Code

15. Supplementary Notes

Langley Research Center Technical Monitor: Claude R. Keckler

Final Report

16. Abstract

The Annular Suspension and Pointing System (ASPS) can provide highly accurate fine pointing for a variety of solar-, stellar-, and Earth-viewing scientific instruments during space shuttle orbital missions. In this report, a detailed nonlinear mathematical model is developed for the ASPS/Space Shuttle system. The equations are augmented with nonlinear models of components such as magnetic actuators and gimbal torquers. Control systems and payload attitude state estimators are designed in order to obtain satisfactory pointing performance, and statistical pointing performance is predicted in the presence of measurement noise and disturbances.

17. Key Words (Selected by Author(s))	18. Distribution Statement
Space shuttle spacelab Magnetic isolation and pointing Experiment fine pointing Sensor systems	Unclassified - Unlimited Subject Category 19

19. Security Classif. (of this report)	20. Security Classif. (of this page)	21. No. of Pages	22. Price*
Unclassified	Unclassified	60	$5.25

*For sale by the National Technical Information Service, Springfield, Virginia 22161.

NASA-Langley, 1978

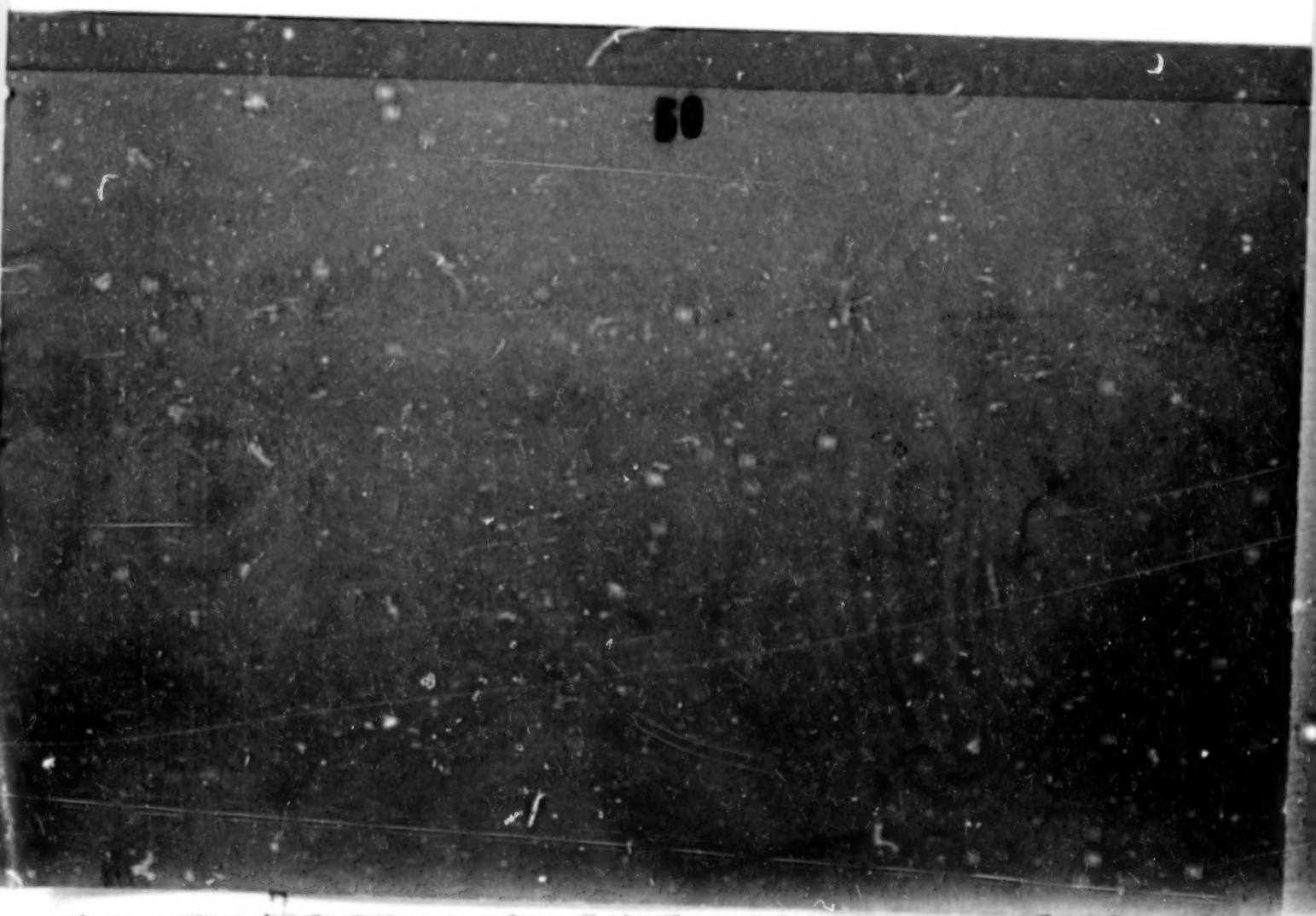
50

END

NOV 2 8 1979